Surface Horizontal Kinetic Energy Distributions Sensitivity to Numerical Parameters in the Tidal-Resolving North and Equatorial Atlantic Derived from Surface Drifter Observations and High-Resolution Numerical Models with Tidal Forcing Simulations

Rémi Laxenaire[1,2], Eric P. Chassignet[2], Xiaobiao Xu[2], Alan J. Wallcraft[2], Luna Hiron[2,3], Brian K. Arbic[4], Maarten C. Buijsman[5], Miguel Solano[5], and Shane Elipot[6]

[1]Laboratoire de l'Atmosphère et des Cyclones (LACy), UMR8105 (Université de la Réunion - CNRS - Météo-France), Université de La Réunion, Saint-Denis de La Réunion, France.
[2]Center for Ocean-Atmospheric Prediction Studies, Florida State University, Tallahassee, FL, USA.
[3]Royal Netherlands Meteorological Institute (KNMI), De Bilt, The Netherlands.
[4]Department of Earth and Environmental Sciences, University of Michigan, Ann Arbor, MI, USA.
[5]School of Ocean Science and Engineering, University of Southern Mississippi, Hattiesburg, MS, USA.
[6]Rosenstiel School of Marine, Atmospheric, and Earth Science, University of Miami, Miami, FL, USA.

Correspondence: Rémi Laxenaire (remi.laxenaire@univ-reunion.fr)

Abstract.

Surface horizontal kinetic energy (SHKE) reflects the distribution of ocean circulation across temporal and spatial scales, shaping energy transfer and mixing in the upper ocean. Quantifying both total SHKE and its frequency content helps characterize processes from low-frequency motions to tides and near-inertial waves, but SHKE variability is difficult to quantify with observations alone. High-resolution tidal-resolving ocean models can bridge gaps in our understanding, yet the modeling results depend on the realism of the configuration choices. Focusing on the In this study, we isolate the role of individual model parameters by comparing seven tidal-resolving HYCOM simulations of the North and Equatorial Atlantic, we compare surface drifter observations to seven HYCOM high-resolution simulations. We assess model parameters that influence KE across the frequency bands. We first quantify the impact of a Lagrangian versus Eulerian framework in interpreting the KE variability and then perform a series of experiments to quantify the sensitivity of in which only one parameter is varied at a time. Surface drifters serve as the observational reference and numerical drifters are seeded in the reference experiment to quantify the distortion of the KE distribution to parameter choices. These low frequency and tidal variance introduced by the Lagrangian sampling. This framework allows a controlled sensitivity analysis of the SHKE distribution across four frequency bands, separately for deep ocean and continental shelf waters. The experiments show that, within the range of configuration changes explored, horizontal resolution is the dominant control for the offshore KE, strongly increasing total and semidiurnal KE, while of offshore total SHKE whereas vertical refinement has a smaller impact offshore , and a stronger impact and a slightly stronger one on the shelf. High-frequency wind forcing Hourly wind forcing strongly amplifies the diurnal and near-inertial variability, while finer bathymetry increases the semidiurnal energy. In contrast, adding wave drag reduces the offshore energy only below the critical latitudes . Overall, the in-depth quantification of the sensitivity of the modeled total KE finer bathymetry enhances the offshore semidiurnal energy, and internal wave drag controls the tidal-band energy equatorward of their critical latitudes while leaving the low-frequency motions nearly unchanged. Increasing the number of tidal-constituent from one (M_2) to eight of the largest constituents sharply

increases the diurnal SHKE and allows us to disentangle the tidal from the non-tidal fraction of the diurnal cycle. Taken together, these experiments show that the shelf and offshore subdomains respond differently to each parameter and that each frequency band is sensitive to a different set of parameters. These results quantify how the configuration choices shape the modeled total SHKE and its spectral distributionto the parameters offers , and offer guidance for setting up high-resolution tide-resolving model experiments.

1 Introduction

Advances in observations and remote sensing have dramatically improved the characterization of ocean velocity fields. For example, geostrophic velocities derived from altimetry provide a global perspective on the geostrophic component of the surface kinetic energy, and have yielded important insights into large-scale to mesoscale motions and their variability (Le Traon, 2013; Abdalla et al., 2021). However, despite recent advances such as the Surface Water and Ocean Topography (SWOT) mission (Morrow et al., 2019; Fu et al., 2024; Archer et al., 2025; Villas Bôas et al., 2025), the spatial and temporal resolution of altimetry remains too coarse insufficient to fully resolve smaller oceanographic features and higher frequency motions ($<$100 km, $< days$). Observations of velocities from ADCPs and drifters can capture higher-frequency motions ($\sim hourly$), but these observations are typically limited in duration and geographically sparse.

The advancement of computational capacity has allowed large-scale high-resolution numerical models to include sub-mesoscale motions (Chassignet and Xu, 2017; Ajayi et al., 2020, 2021; Chassignet et al., 2023) and tides (Arbic et al., 2012, 2018; Buijsman et al., 2020; Arbic, 2022; Xu et al., 2022). Numerical models therefore provide a complementary tool to study processes at high temporal and spatial resolution. These models are particularly relevant for the study of high-frequency motions such as internal tides, near-inertial waves, and motions spanning quasi-inertial to low-frequency motions. However, numerical models are, by construction, truncated representations of the ocean, and the modeled circulation is strongly dependent on parameter choices, such as mixing parameterizations and/or horizontal and vertical resolution (e.g., Chassignet and Xu, 2017; Buijsman et al., 2020; Chassignet et al., 2023; Xu et al., 2023; Hiron et al., 2025; Buijsman et al., 2025).

Spectral decomposition of surface currents provides a powerful framework to separate and analyze the distribution of surface horizontal kinetic energy (SHKE) across physically meaningful frequency bands. This approach enables the investigation of key interactions (e.g., wave–current coupling, nonlinear wave–wave transfers), the pathways of energy across scales, and even the tuning of model parameters. Elipot and Lumpkin (2008) and Elipot et al. (2016) first applied rotary spectra to drifter observations, decomposing SHKE into anticyclonic and cyclonic components that could be mapped into distinct reservoirs of variability to quantify the near surface variability on global scales. Extending this method to model–observation comparisons, Yu et al. (2019) compared a global MIT General Circulation Model (MITgcm) simulation (LLC4320) to surface drifters in waters deeper than 500 m and demonstrated that surface drifters are an efficient database for assessment of the surface circulation predicted by a tide- and eddy-resolving global ocean model. Indeed, they found similar qualitative patterns in SHKE in both the model and observations, with a dominance of low frequencies and well-defined tidal and near-inertial peaks. Quantitative differences, however, emerged, such as energy deficit (e.g., at low latitudes, and at the near-inertial frequency)

or excess (e.g., at the semidiurnal frequency) in the model relative to the observations. Subsequently, Arbic et al. (2022) compared the near-surface SHKE of another high-resolution global simulation performed with the Hybrid Coordinate Ocean Model (HYCOM) to that of the MITgcm LLC4320 and the drifters' SHKE. The analysis focused on the vertical structure of the near-surface current by comparing results at the surface with those at 15 m depth. They found significant vertical structure differences between surface and 15 m velocities in all frequency bands, except the semidiurnal band. The same energy deficit as in Yu et al. (2019) remained present in the models near the equator when compared to observations, but the lack of energy at the near-inertial frequency is was less pronounced in HYCOM than in the MITgcm. In addition, the HYCOM semidiurnal SHKE was found to be closer to those estimates derived from surface drifter observations than the MITgcm semidiurnal SHKE . Although both Yu et al. (2019) and Arbic et al. (2022) put forward several explanations for the differences between the modeled KE and the KE SHKE and the SHKE derived from surface drifter data, they acknowledged the inherent difficulty of comparing fields derived from Eulerian (models) and Lagrangian (observations) velocities. Arbic et al. (2022) also pointed out several limitations in their ocean model comparison, i.e., different forcing and numerical parameters (e.g., vertical grid resolution, frequency of atmospheric wind forcing, presence or absence of wave drag), outputs from different years, and systematic model errors (e.g., issues with the tidal forcing in the MITgcm LLC4320 simulation). These limitations illustrate the difficulty of disentangling the respective roles of individual parameters when simulations differ simultaneously in multiple aspects, leaving open the question of which choices most strongly shape the modeled SHKE.

The differences between Eulerian and Lagrangian estimates of KE were recently investigated by Zhang et al. (2024) and ?In addition to parameter-related uncertainties, there is the distortion in SHKE that arises when estimating the low frequency and tidal variance from drifters (Zhang et al., 2024; Caspar-Cohen et al., 2025). Zhang et al. (2024) systematically compared Eulerian and Lagrangian estimates of SHKE by seeding a large ensemble of numerical drifters into the global MITgcm LLC4320 using the v2.0 *Parcels* Python package (Lange and Van Sebille, 2017; Delandmeter and Van Sebille, 2019) and showed that Lagrangian velocity spectra are generally smoother and tend to underestimate SHKE at low-frequency and in tidal bands, particularly in regions with strong low-frequency KE. ? showed that one needs to take into account the distortion introduced by the drifting nature of surface drifters when comparing SHKE. Caspar-Cohen et al. (2025) systematically compared the Lagrangian and Eulerian frequency distributionsin LLC4320 . Their analysis of the semidiurnal KE levels in the MITgcm LLC4320 and HYCOM simulations are consistent with those and confirmed the findings of Yu et al. (2019) and Arbic et al. (2022), i.e., that the semidiurnal energy in MITgcm LLC4320 is, on average, about twice that of in situ observations, while the observed values and that HYCOM shows relatively minimal bias overall, though regional variations are apparent.

In this paper, we build on summary, the above studies (Yu et al., 2019; Arbic et al., 2022; Zhang et al., 2024; ?) to investigate in depth the impact of highlight two main sources of ambiguity in their model–observation comparisons of SHKE: the simultaneous variation of multiple parameters between simulations, which prevents a clean attribution of SHKE differences to any specific choice, and the distortion introduced by Lagrangian sampling, which complicates the direct use of drifter observations as a reference. In this paper, we remove these ambiguities by (a) analyzing a series of experiments in which only a single parameter is varied at a time and (b) using numerical drifters to evaluate the level of agreement between the model and the observations and to quantify the bias arising from Lagrangian sampling. The central objective of the paper is to isolate and quantify the impact of the choices in numerical and forcing parameters on the modeled surface KE. Following the approach of Arbic et al. (2022),

we use SHKE. This is achieved by relying on a suite of tidal-resolving HYCOM simulations of the North and Equatorial Atlantic (Table 1) together with numerical particle experiments, to address several of the limitations that they identified in their study. Specifically, we rely on model–model comparisons between twin experiments, where only a single parameter is varied at a time. This design that allows us to isolate the impact of directly attribute SHKE differences to (a) grid resolution (horizontal and vertical), (b) bathymetry resolution, (c) forcing (wind frequency and tidal content), and (d) wave dragand quantify the differences in KE that can be directly attributed to each factor. We also separate our analysis between . This framework also enables us to extend the analysis from offshore/deep ocean waters (deeper than 500 m)and , covered by previous drifter-based comparisons, to inshore/continental shelf waters (shallower than 500 m). In parallel, we use numerical drifters to further quantify the differences between Lagrangian and Eulerian sampling of velocity fields. The numerical drifters allow us to bridge the two perspectives and link , where the high-frequency SHKE is of particular importance, a region that surface drifter-based comparisons could not cover due to the lower density of observations. The Lagrangian comparison enables us to link the Eulerian-based sensitivity results to observations. Together, these steps provide a clearer attribution of parameter effects, reducing ambiguities in model –observation comparisons, and offering guidance for configuring tide-resolving models capable of reproducing high-frequency surface KEdirectly to observations, without conflating genuine model biases with Lagrangian-Eulerian sampling differences.

The article is organized as follows: Section 2 describes the configurations of the seven HYCOM simulations, the implementation of the numerical drifters, and the surface drifter database used in the comparison. It also introduces the method used to calculate the rotary spectra. In section Section 3, the surface domain averaged KE domain-averaged SHKEs from all Eulerian and Lagrangian datasets (numerical and observed) is compared . are compared within a common framework, providing a global view of the datasets and identification of the spectral features they share. This section serves as the baseline for the comparisons performed in the following sections. In Section 4, the Lagrangian spectral estimates from the numerical drifter experiments are (a) compared with that of the surface drifter observations , (b) used to assess the impact of sampling density, and (c) compared with the experiment are compared to the drifter observations and to the Eulerian model outputs. In section This section provides the link between the surface drifter observations and the Eulerian experiments analyzed in the following section. Section 5 , systematically quantifies the impacts of the configuration and parameter choices is quantified listed above on the SHKE using the Eulerian frequency rotary spectra, with separate analyses conducted for deep ocean and continental shelf waters. Specifically, we systematically investigate the impact on the modeled surface KE of the horizontal and vertical resolutions, the number of tidal components, the wave drag, the spatial resolution of the bathymetry, and finally the temporal frequency of wind forcing. By contrasting these experiments with each other, we can directly attribute KE differences to specific changes made between experiments. Finally, the results are summarized in the concluding section, where we rank the parameters with the most noticeable impact for each frequency band and discuss their relative importance. The final section synthesizes the results by discussing the parameters that most strongly affect the SHKE distribution in each frequency band and by addressing which one could be adjusted to reduce the model-drifter gap.

2 Data and methods

This section describes the datasets and methods used throughout this study. All analyses are conducted within the North and Equatorial Atlantic (NEATL) domain, which extends from 28°S to 80°N (Figure 1a). The domain is divided into two subdomains: offshore/deep ocean waters and inshore/continental shelf waters, defined as $1° \times 1°$ cells whose

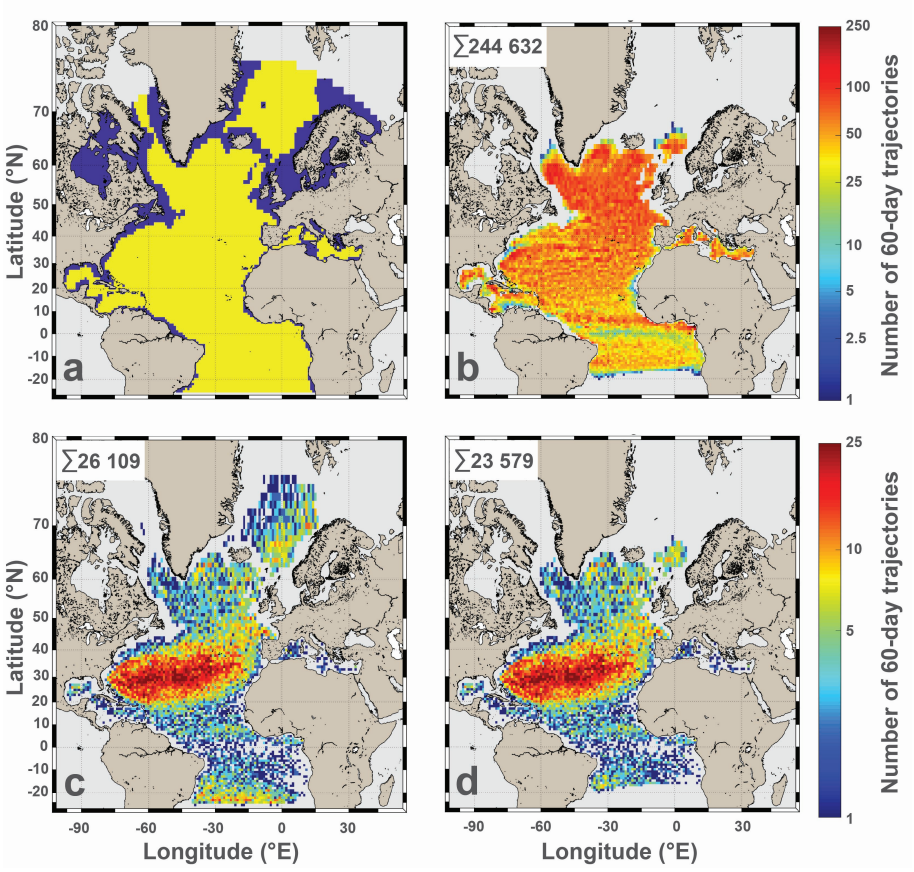

Figure 1. (a) HYCOM NEATL domain in $1^\circ \times 1^\circ$ bins of yellow (blue) regions indicating offshore (inshore) regions in waters deeper (shallower) than $500\,m$. (b)-(d) Number of 60-day trajectory segments per $1^\circ \times 1^\circ$ offshore bin for (b) the full OceanParcels experiment (OP Seed 1/2°), (c) the undrogued surface drifter observations, and (d) the subsampled OceanParcels experiment (OP Seed Drifters), constructed to reproduce the spatial sampling of the observed undrogued drifters. The total number of segments is indicated in the upper-left corner of panels b to d.

median depth, estimated from the ETOPO1 database (Amante and Eakins, 2009), exceeds or is shallower than $500\,m$ respectively. These two subdomains represent approximately 77% and 23% of the total NEATL domain area, respectively.

2.1 Ocean Surface Drifters

We use version 2.01 of the hourly data set from the Global Drifter Program (Elipot et al., 2016, 2022) which includes $15\,m$-drogued and undrogued drifters. It is important to note that the positioning system used to track the drifters (Argos or GPS) can have an impact on the power spectral density of velocity. Yu et al. (2019) showed that the noise in the Argos positioning system adds high-frequency energy when compared to surface buoys equipped with GPS. In the HYCOM North and Equatorial Atlantic

(NEATL) domain NEATL domain (Figure 1a), the database of undrogued (drogued) drifters, which was downloaded on 30 April 2025, can be divided into 27,134 (25,956) continuous 60 day 60-day segments, each associated with its mean position over the segment duration(Figure 1c). Among these, 11,591 (14,933) of these are are from GPS-tracked drifters. Of the segments of both Argos and GPS-tracked undrogued (drogued) drifters, 26,109 (23,704), corresponding to 96% (91%) of the total, are located in offshore waters, reflecting the sparse coverage of surface drifters in coastal regions. Because SHKE is defined at the ocean surface, we focus on undrogued drifters in the following analyses, as they more accurately sample surface velocities (Niiler and Paduan, 1995; Lumpkin and Pazos, 2007). Undrogued drifters are known to carry a larger wind-slip error than drogued ones, reaching 8.6 $10^{-2}\ m\,s^{-1}$ per 10 $m\,s^{-1}$ wind speed compared to 0.7 $10^{-2}\ m\,s^{-1}$ downwind per 10 $m\,s^{-1}$ wind speed for drogued drifters (Niiler and Paduan, 1995), but this slip has not yet been comprehensively disentangled from genuine oceanic surface variability across frequencies (see Arbic et al., 2022, for a discussion of the limitations of using undrogued versus drogued drifters for model comparison). The number of undrogued drifter segments per $1^\circ \times 1^\circ$ cell in the offshore domain is shown in Figure 1c. The spatial distributions of the other drifter datasets (drogued and undrogued, GPS-tracked and all) are provided in Figure S1 in the supplementary material.

2.2 HYbrid Coordinate Ocean Model (HYCOM) simulations

The North and Equatorial Atlantic (NEATL) NEATL HYCOM experiments, covering the Atlantic from 28°S to 80°N (Figure 1a), are part of a suite of eddying and submesoscale-enabled numerical simulations performed by co-authors with HYCOM v2.3.01 (Bleck, 2002; Chassignet et al., 2003, 2009). These simulations (Chassignet and Xu, 2017; Xu et al., 2022; Chassignet et al., 2023; Xu et al., 2023) were performed to study and quantify the impact of horizontal and vertical resolution on the large-scale circulation and water mass transformations in the Atlantic. In this paper, we analyze three 1/12° horizontal grid-spacing configurations (9 km at the equator, 6 km in the Gulf Stream region) and four 1/50° horizontal grid-spacing configurations (2.25 km at the equator, 1.5 km in the Gulf Stream region). Three of these configurations have been used previously in Xu et al. (2022), while four simulations (NEATL12-T, NEATL12-M_2, NEATL12-T-HVR, and NEATL50-T-WD) are analyzed for the first time. All the The simulations are integrated for 18 months with tidal forcing of the eight largest tidal constituents (K_1, O_1, P_1, Q_1, M_2, S_2, N_2, and K_2) after spin-up as described in Xu et al. (2022). The last 12 months outputs are used in the analysis.

These simulations are listed in Table 1, but are described in more details in the following:

- NEATL12-T is the tidal 1/12° reference simulation with 6-hourly atmospheric forcing and 8 tidal constituents.
- NEATL12-M_2 is a twin experiment of NEATL12-T, but with only the semidiurnal tidal constituent (M_2, 1.932 cycles per day (cpd)).
- NEATL12-T-HVR is a twin experiment of NEATL12-T, but with 96 vertical coordinates instead of 32.
- NEATL50-T is a twin experiment of NEATL12-T, but with a 1/50° horizontal grid-spacing and a coarse bathymetry linearly interpolated from the 1/12° grid-spacing topography of the NEATL12-T (Chassignet and Xu, 2017; Xu et al., 2022; Chassignet et al., 2023). NEATL12-T's bathymetry is based on the 2' Naval Research Laboratory digital bathymetry

database, which combines the global topography based on satellite altimetry of Smith and Sandwell (1997) with several high-resolution regional databases.

- NEATL50-T-WD is a twin experiment of NEATL50-T. However, instead of having no wave drag as in NEATL50-T, a Jayne and St. Laurent (2001) internal wave drag with a multiplicative factor of 0.25 is applied to the bottom of the water column (we refer to Buijsman et al. (2015) and Buijsman et al. (2020) for a discussion of this parameter).

- NEATL50-T-HB is a twin experiment of NEATL50-T, but with a 1/50° bathymetry that is derived from the 2019 version of the 15 arc-seconds General Bathymetric Chart of the Ocean data set (GEBCO Bathymetric Compilation Group 2019, 2019) as in Chassignet et al. (2023).

- NEATL50-T-HB-HF is a twin experiment of NEATL50-T-HB, but with higher-frequency, hourly wind stress variability from the National Centers for Environmental Prediction Climate Forecast System Reanalysis (Saha et al., 2010) instead of the 6-hourly wind forcing used in previous experiments.

In the vertical dimension, the above simulations contain 32 or 96 hybrid layers with density referenced to 2,000 m (σ_2) (see Chassignet and Xu (2017) and Xu et al. (2023) for details). The vertical coordinate (Bleck, 2002) is isopycnal in the stratified open ocean and makes a dynamically smooth and time dependent transition to terrain-following coordinates in shallow coastal regions and to fixed pressure levels in the surface mixed layer and/or unstratified seas (Chassignet et al., 2003, 2006). No inflow or outflow is prescribed at the northern and southern boundaries. Within a buffer zone of about 3° from the northern and southern boundaries, the 3-D modeled temperature, salinity, and depth of isopycnal interfaces are restored to the monthly Generalized Digital Environmental Model (GDEM, Teague et al. (1990); Carnes (2009)) (GDEM, Teague et al., 1990; Carnes, 2009) climatology with an e-folding time of 5-60 days that increases with distance from the boundary. The initial conditions are derived from the GDEM climatology potential temperature and salinity and the atmospheric forcing is derived from the European Centre for Medium-Range Weather Forecasts reanalysis ERA40 (Uppala et al., 2005) with 6-hourly wind anomalies from the Fleet Numerical Meteorology and Oceanography Center Navy Operational Global Atmospheric Prediction System (Hogan and Rosmond, 1991; Goerss and Jeffries, 1994) for the year 2003. The year 2003 is considered a neutral year over the 1993-present timeframe in terms of long-term atmospheric patterns, such as the North Atlantic Oscillation. The reader is referred to Chassignet and Xu (2017) and Chassignet et al. (2023) for details on the parameterizations used in the model.

To derive surface velocity from particles, and thus simulate the trajectories of surface drifters, we performed an Ocean Parcel OceanParcels experiment using the v2.3.1 .2 *Parcels* Python package (Lange and Van Sebille, 2017; Delandmeter and Van Sebille, 2019). This Ocean Parcel (Lange and Van Sebille, 2017; Delandmeter and Van Sebille, 2019; Van Sebille et al., 2021). This OceanParcels experiment (hereafter referred to as OP Seed 1/2°) was conducted in offline using hourly 2D advecting velocity field (a combination of ocean current and wind-wave effects) outputs from the NEATL50-T-HB-HF numerical simulation. Particles were seeded every 30 days on a regular 1/2° × 1/2° regular grid and grid between 15°S and 65°N in the NEATL domain and are advected with *Parcels* using a fourth-order Runge-Kutta scheme and no stochastic diffusion. The latitudinal restrictions were imposed to avoid proximity to the model open boundaries (located near 28°S and 80°N at the Fram Strait); the

Table 1. Summary of the seven North and Equatorial Atlantic (NEATL) HYCOM simulations (updated from Xu et al. (2022))

Experiment	Horizontal resolution	Number of layers	Bathymetry resolution	Atmospheric forcing frequency	Number of Tidal constituents	Wave drag
NEATL12-T	1/12°	32	1/12°	6 hours	8	No
NEATL12-M_2	1/12°	32	1/12°	6 hours	1	No
NEATL12-T-HVR	1/12°	96	1/12°	6 hours	8	No
NEATL50-T	1/50°	32	1/12°	6 hours	8	No
NEATL50-T-WD	1/50°	32	1/12°	6 hours	8	Yes
NEATL50-T-HB	1/50°	32	1/50°	6 hours	8	No
NEATL50-T-HB-HF	1/50°	32	1/50°	1 hour	8	No

(a) HYCOM NEATL domain in $1^\circ \times 1^\circ$ bins of yellow (blue) regions indicating offshore (inshore) regions in waters deeper (shallower) than 500 m. (b) and (c) number of 60-day trajectories in $1^\circ \times 1^\circ$ bin for, respectively, the Ocean Parcel experiment and undrogued surface drifters. The total number of segments is given in the top left of panels b and c.

northern limit of 65°N also corresponds approximately to the Greenland-Scotland Ridge, which forms a natural boundary of the North Atlantic basin. Trajectories were then tracked for 60 days . This resulted resulting in 11 seeding events over the one-year simulation , and yielding 264,361 trajectory segments of 60 days,each associated with its mean position over segment duration (which 244,632 (92%) are located in offshore waters (Figure 1b).

To assess whether differences between simulated and observed statistics could arise solely from the irregular spatial distribution of real drifter observations, we constructed a subset of the OP Seed 1/2° dataset that replicates the sampling characteristics of the undrogued surface drifter dataset (hereafter referred to as OP Seed Drifters; Figure 1d). Specifically, for each 1° 1° × 1° 1° bin cell of OP Seed 1/2°, we randomly selected trajectory segments so such that the number of simulated segments in that cell match each cell matches the number of undrogued surface drifter segments observed in the same cell (Figure 1cd). In a few cases, close to northern and southern limits, the OP Seed 1/2° dataset contained fewer segments than the undrogued drifter dataset for a given cell; in such cases, all available simulated segments were used. This approach keeps the spatial sampling density of the OP Seed Drifters as close as possible to that of the observational datasetwhile avoiding oversampling, ensuring that any differences found in subsequent analyses cannot be attributed to sampling bias. The resulting subset contains 24,302 trajectory segments of 60 days each. , of which 23,579 (97%) are located in offshore waters (Figure 1d).

Finally, we divide the NEATL domain into offshore/deep ocean waters and inshore/continental shelf waters (Figure 1a) . These sub domains are defined, respectively, as grid points in waters deeper and shallower than 500 m as interpolated from ETOPO1 database (Amante and Eakins, 2009). Yu et al. (2019), Arbic et al. (2022), and Zhang et al. (2024) restricted their analysis to the deep ocean because the geographical distribution of drifters is quite sparse near the coast (Figures 1b,c). For that reason, we also constrain our Lagrangian analysis to the offshore domain. However, when computing the Eulerian fields, both offshore and inshore domains are considered and discussed.

2.3 Analysis methods

Building upon the methodologies outlined in Yu et al. (2019), Arbic et al. (2022), and Zhang et al. (2024), frequency rotary spectra (Gonella, 1972; Mooers, 1973) at each model grid point (Eulerian) and along drifter trajectories (Lagrangian) are computed from surface horizontal velocity time series taken from the HYCOM simulation and surface drifter data. Rotary velocity spectra break down velocity variance into contributions from different frequencies and also separate clockwise from counterclockwise components, thereby distinguishing anticyclonic from cyclonic energy. Following Yu et al. (2019) and Arbic et al. (2022), velocity variance is estimated and interpreted as KEkinetic energy; no factor of $1/2$ is included in the calculations.

To compute spectra, hourly velocity time series (generated at each grid point for the Eulerian estimate and derived from particle velocities for the Lagrangian estimate) are segmented into 60-day periods with a 50% overlap and linearly detrended. For both the model and drifter data, complex-valued fields ($u + iv$, where u and v represent zonal and meridional velocity components, respectively) are multiplied by a Hanning window before computing the 1-D discrete Fourier transform. Spectral estimates are obtained by multiplying the Fourier coefficients by their complex conjugates and averaged over segments. Finally, as per Yu et al. (2019), the rotary frequency spectral densities are adjusted by a factor of $8/3$ to account for the windowing operation (Emery and Thomson, 2001). The resulting Power Spectral Density (PSD) of the rotary spectra corresponds to a 1-year period for the numerical products (both Eulerian and Lagrangian) and spans more than 30 years for the surface drifters (from the end of the 1980s to the beginning of the 2020s).

To decompose SHKE , the velocity rotary spectra are integrated over four frequency bands: high-frequency ($<$ -0.5 cpd and $>$ 0.5 cpd, with cpd stands for cycles per day), near-inertial ($\pm$[0.9, 1.1]f cpd, excluding the $\pm 5^\circ$ latitude band around the equator, with f the Coriolis parameter), semidiurnal ($\pm$[1.9, 2.1] cpd), and diurnal ($\pm$[0.9, 1.1] cpd). In addition to these estimated SHKE components, the total SHKE (i.e., the time-mean of the instantaneous values squared) and low-frequency KE (total KE SHKE (total SHKE minus high-frequency SHKE) are computed. It is worth noting that in Arbic et al. (2022), SHKE maps from drifters were obtained slightly differently: the authors band-pass or low-pass filtered the drifter velocity time series and then computed the variance of the filtered velocities within bins. As stated by Arbic et al. (2022), both methods (Yu et al., 2019; Arbic et al., 2022) yield similar results. This allows us to use the same approach for both Eulerian and Lagrangian fields.

Finally, the spectra and SHKE are averaged within $1^\circ \times 1^\circ$ cells and the $1^\circ \times 1^\circ$ cells in the NEATL domain. Given that the vast majority of Lagrangian segments (96% of undrogued drifters and 92% of OP segments) are located in offshore waters, the Lagrangian analysis is constrained to the offshore domain, consistently with Yu et al. (2019), Arbic et al. (2022), and Zhang et al. (2024). For the Eulerian fields, both subdomains are considered. The resulting gridded rotary spectra and SHKE partitions produced for this study are archived at SEANOE (NetCDF and associated README; (Laxenaire et al., 2026)Laxenaire et al. (2026)).

3 Domain averaged surface kinetic energy distributions

In this section, we analyze the surface rotary velocity spectra and KE surface horizontal kinetic energy (SHKE) integrated over selected frequency bands and over the entire NEATL domain. The $1^\circ \times 1^\circ$ gridded spectra and SHKE are averaged

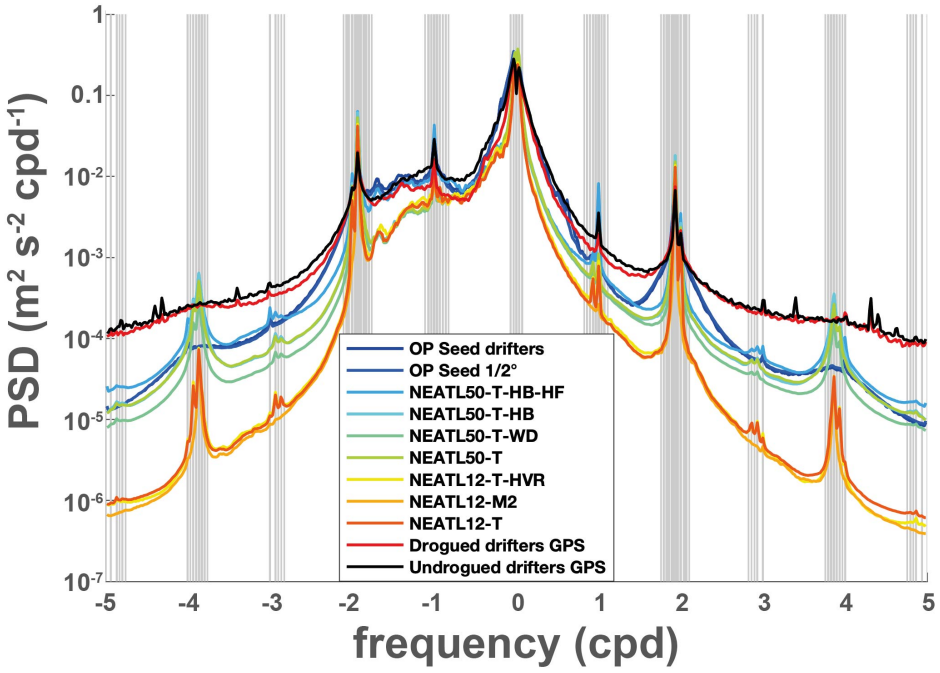

Figure 2. Rotary spectra of surface horizontal kinetic energy averaged over offshore regions for the NEATL domain between -5 and 5 cycles per day (cpd) from the HYCOM simulations, Ocean Parcel OceanParcels (OP) experiments and from surface drifters. Cyclonic and anticyclonic motions are assigned to positive and negative frequencies, respectively. The vertical gray lines indicate tidal frequencies in both positive and negative frequency domains from Arbic et al. (2022). Note the decimal logarithmic scale for the Power Spectrum Density (PSD).

using weights proportional to the surface area of each cell, separately for the offshore and continental shelf subdomains (Figure 1a). This analysis provides the baseline for the subsequent detailed comparisons between observed and modeled drifters, Lagrangian and Eulerian estimates, and the twin numerical experiments. The $1^\circ \times 1^\circ$ gridded spectra and KE are first averaged over the domain using weights proportional to the surface area of each cell. numerical sensitivity experiments.

The rotary spectra for the observed surface drifters, the Ocean Parcel OceanParcels numerical drifters, and the seven HYCOM simulations, computed and averaged over the NEATL offshore domain (depth greater than 500 m), are displayed in Figure 2. We focus on the offshore domain because the coverage by the observed drifters is sparse in depths less than 500 m. The overall pattern is the same for allwith a decreasing kinetic energy similar for all, with higher energy levels at low frequencies, forming a broad peak, and with kinetic energy decreasing as the absolute value of the frequency increases and with high energy pronounced peaks at the tidal forcing frequencies. Except for the Within the ± 2 cpd range, the spectra are not symmetric about zero frequency, with consistently more energy on the anticyclonic domain (assigned to negative frequencies in Figure 2), reflecting the predominance of the anticyclonic near-inertial oscillations. All Eulerian estimates exhibit peaks at the tidal frequencies (gray lines in Figure 2), with the exception of NEATL12-M_2experiment, which is forced solely by the M_2 tidal constituent , the Eulerian estimates have the same number of peaksin

Table 2. Surface horizontal kinetic energy (KE; $10^{-3}\ m^2\ s^{-2}$SHKE) averaged over the NEATL domain for the seven HYCOM experiments, the Ocean Parcel OceanParcels (OP) experiments, and surface drifters. Two For both types of surface drifters (drogued and undrogued), two datasets are considered, one that includes GPS-tracked drifters only and one with all drifters (both Argos and GPS positioning systems). Presented below are the total KESHKE, and KE integrated over percentage of the total SHKE stored in low-frequency ($>$ -0.5 cpd and $<$ 0.5 cpd); diurnal frequency ($\pm$[0.9, 1.1] cpd); semidiurnal frequency ($\pm$[1.9, 2.1] cpd); and near-inertial frequency ($\pm$[0.9, 1.1]f cpd poleward of $\pm$ 5° latitude) reservoirs (See Table S1 in the supplementary for absolute value of SHKE in each reservoirs). Each cell shows KEdSHKEd/KEs SHKEs where KEd SHKEd and KEs SHKEs represent KE SHKE values computed in waters deeper and shallower than 500 m, respectively. KEs SHKEs are not provided for Lagrangian fields (i.e., OP and drifters) due to the low density of observations in these regions (Figure 1).

Experiment	Total $[10^{-3}\ m^2\ s^{-2}]$	Low freq % Total	Diurnal % Total	Semidiurnal % Total	Near-Inertial % Total
NEATL12-T	96.8/134.1	88.8/61.2 91.8/45.7	1.3/2.0 1.3/1.5	1.8/64.4 1.9/48.0	5.9/27.2 6.1/20.3
NEATL12-M_2	98.1/126.3	90.7/61.5 92.4/48.7	1.1/0.6 1.1/0.5	1.6/60.1 1.7/47.6	5.8/25.5 5.9/20.2
NEATL12-T-HVR	107.0/151.1	98.4/69.1 91.9/45.7	1.4/2.1 1.3/1.4	1.9/72.4 1.8/47.9	6.4/27.7 5.9/18.3
NEATL50-T	127.2/144.5	117.3/71.8 92.2/49.7	1.3/2.2 1.0/1.5	2.6/62.7 2.0/43.4	5.3/26.0 4.2/18.0
NEATL50-T-WD	124.8/140.8	116.4/70.9 93.2/50.4	1.2/2.1 1.0/1.5	1.9/60.3 1.6/42.9	5.1/25.2 4.1/17.9
NEATL50-T-HB	118.0/136.3	107.9/61.3 91.4/45.0	1.3/2.0 1.1/1.4	3.0/65.5 2.5/48.0	5.3/25.2 4.5/18.5
NEATL50-T-HB-HF	125.1/143 .0	108.5/64.1 86.7/44.8	3.0/3.2 2.4/2.2	3.2/65.2 2.6/45.6	9.5/27.6 7.6/19.3
OP Seed 1/2°	122.6/–	107.7/– 87.8/–	3.1/– 2.5/–	2.1/– 1.7/–	9.3/– 7.6/–
OP Seed drifters	122.7/–	101.5/– 83.3/–	3.3/– 2.7/–	2.1/– 1.7/–	9.9/– 8.0/–
Undrogued drifters	137.8/–	103.7/– 75.3/–	2.8/– 2.0/–	1.7/– 1.2/–	8.1/– 5.9/–
Undrogued drifters GPS	146.3/–	94.1/– 64.3/–	3.1/– 2.1/–	1.8/– 1.2/–	8.4/– 5.8/–
Drogued drifters	99.8/–	77.8/– 78.0/–	1.9/– 1.9/–	1.7/– 1.7/–	6.8/– 6.8/–
Drogued drifters GPS	101.7/–	74.5/– 74.5/–	1.8/– 1.8/–	1.9/– 1.9/–	7.3/– 7.2/–

Same as in Table **??** but the domain-averaged surface kinetic energy stored in the different reservoir is expressed as a percentage of the total energy, with values separated between waters deeper and shallower than 500 m. Note that the sum of percentages can exceed 100% because the individual frequency bands are derived from velocity variance interpreted as KE. Experiment Low freq Diurnal Semidiurnal Near-Inertial NEATL12-T 91.8%/45.7% 1.3%/1.5% 1.9%/48.0% 6.1%/20.3% NEATL12-M_2 92.4%/48.7% 1.1%/0.5% 1.7%/47.6% 5.9%/20.2% NEATL12-T-HVR 91.9%/45.7% 1.3%/1.4% 1.8%/47.9% 5.9%/18.3% NEATL50-T 92.2%/49.7% 1.0%/1.5% 2.0%/43.4% 4.2%/18.0% NEATL50-T-WD 93.2%/50.4% 1.0%/1.5% 1.6%/42.9% 4.1%/17.9% NEATL50-T-HB 91.4%/45.0% 1.1%/1.4% 2.5%/48.0% 4.5%/18.5% NEATL50-T-HB-HF 86.7%/44.8% 2.4%/2.2% 2.6%/45.6% 7.6%/19.3% OP Seed 1/2° 87.8%/– 2.5%/– 1.7%/– 7.6%/– OP Seed drifters 82.7%/– 2.7%/– 1.7%/– 8.1%/– Undrogued drifters 75.3%/– 2.0%/– 1.2%/– 5.9%/– Undrogued drifters GPS 64.3%/– 2.1%/– 1.2%/– 5.8%/– Drogued drifters 78.0%/– 1.9%/– 1.7%/– 6.8%/– Drogued drifters GPS 74.5%/– 1.8%/– 1.9%/– 7.2%/–

the ±5 cpd frequency rangeconstituent and therefore lacks the other tidal peaks. The peaks in KE at the SHKE at higher frequencies are either absent or less marked in the Lagrangian databases datasets (i.e., observed and numerical drifters), in agreement with Arbic et al. (2022). The most notable differencesamong the datasets is lies in the level of energy in the high-frequency internal gravity wave continuum (Garrett and Munk, 1975) with the highest energy values in the observed drifters datasets(drogued and undrogued) and the lowest in the coarse-resolution 1/12° horizontal grid-spacing simulations. There is a significant increase of energy in the 1/50° (Lagrangian and Eulerian) horizontal grid-spacing simulations, but they do not reach the level of the observations.

To obtain a quantitative measure of the differences, we also compute the domain-averaged surface KE components SHKE and its distribution across different frequency bands for all datasets(Table ??). We also differentiate between the continental shelf and open ocean as this distinction will become important in subsequent discussions. Furthermore, in . In order to compare variations in energy distribution among datasets that do not have the same total energySHKE, we express the energy in each frequency reservoir as a fraction of the total energy SHKE (Table ??2).

As pointed out by Yu et al. (2019) and Arbic et al. (2022), most of the energy in the offshore domain waters —(deeper than 500 m—) is contained in the low-frequency band, representing 8083–9593% of the total SHKE for the numerical simulations and 6064–7578% for the drifters (Table ??2). This is expected given that large- and mesoscale motions account for most of the oceanic KE kinetic energy (Wunsch and Stammer, 1995; Ferrari and Wunsch, 2009; Morrow and Le Traon, 2012). In contrast, the diurnal, semidiurnal and near-inertial narrower frequency intervals contain between one and two orders of magnitude less energy. Although their fractional contribution is small, high-frequency motions play an important role since they are the main pathways for energy transfer and mixing in the ocean interior (Wunsch and Ferrari, 2004; Müller et al., 2005).

The same variables can be computed in the Eulerian estimates over the continental shelf—When we extend the analysis of Yu et al. (2019) and Arbic et al. (2022) to waters shallower than 500 m. The shelf , the results (Table ??2) are markedly different, with the energy total SHKE being higher on average inshore than offshore and with the low-frequency band accounting for only 45–50% of the total (Table ??2), leaving considerably more energy associated with higher-frequency motions in inshore areas. There is little In the diurnal band, the difference in the energy between offshore and inshore in the diurnal bandvaries across configurations with no consistent pattern, but there is a striking difference in the semidiurnal and near-inertial bands, where . For the semidiurnal band, the continental shelf can contain up to 35 25 times more energy than in the open ocean(Tables ?? and ??fraction than the deep ocean, while the near-inertial band shows a more moderate but still significant enhancement by a factor of 3 to 4 (Table 2 and Table S1 in the supplementary). Tidal shoaling implies that, as water depth decreases, mass conservation requires higher barotropic velocities and hence larger SHKE of the barotropic tide, even if a portion of the barotropic energy is converted into internal tides (see demonstration of a tidal wave crossing a slope without reflection or friction in Pugh and Woodworth, 2014). However, shoaling should affect both the diurnal and semidiurnal bands similarly, which is not what we observe. For instanceIn addition, in the NEATL domain, several shelf and marginal basins exhibit resonant behavior that selectively amplifies tidal components, depending on their geometry. Diurnal resonances occur in regions such as the Gulf of Mexico (e.g., Grace, 1932), whereas semidiurnal resonances are prominent in the Hudson Bay (e.g., Cummins et al., 2010), the North Sea (e.g., Jänicke et al., 2021), the English Channel and Irish Sea (e.g., Webb, 2013), and the Bay of Fundy–Gulf of Maine system (e.g.,

Garrett, 1972). Therefore, area-averaged diagnostics cannot fully explain the differences between offshore and inshore energy frequency decomposition. Assessing how numerical parameter choices affect the spatial distribution of SHKE requires first establishing a reliable observational reference (Section 4), before examining sensitivities through the experimental framework (Section 5).

4 Lagrangian spectral estimates of surface KE

4 Lagrangian spectral estimates of SHKE

Domain-averaged spectra establish the large-scale structure of surface kinetic energy, but mask important regional and experiment-specific differences. The observations are Lagrangian and are inhomogeneous in space and time. The question then arises as to how spectra computed from a Lagrangian perspective differ from an Eulerian perspective and to what extent we can use observations-based spectra as a reference. To address this , we perform a detailed analysis to evaluate the role of sampling density and quantify the differences in Lagrangian and Eulerian estimates. Specifically, we Comparing model outputs to surface drifter observations requires accounting for the distortion in the low frequency and tidal variance introduced by the Lagrangian nature of drifter sampling. To this end, we compare rotary spectra from undrogued drifters with those from numerical particles in the OP Seed Drifters, a subset of numerical particles advected in the NEATL50-T-HB-HF simulation and subsampled to replicate the number and spatial distribution of undrogued drifter segments. NEATL50-T-HB-HF is our "best" 1/50° experiment (fine bathymetry and hourly winds, NEATL-50-T-HB-HF) , which) in the sense that it most closely matches observations in the globally averaged rotary spectra of KE (Figure 2). We then compare the same Lagrangian estimates to their Eulerian counterpart.

4.1 Observed versus numerical drifters

In order to compare the surface-advected numerical particles with observations, we focus on undrogued surface drifters, which better capture surface currents than the drogued drifters that were designed to be advected by subsurface currents (Niiler and Paduan, 1995; Lumpkin and Pazos, 2007). It is important to note that there is noise present in the velocity estimates derived from both the GPS- and Argos-tracked drifters. The Argos-tracked drifters exhibit higher noise levels and thus more strongly affect the PSD of rotary spectra Yu et al. (2019). In In Figure 2, only the the GPS-tracked drifters were used to minimize the noise impact while, in the rest of this section (Figures **??** and **??**), (Yu et al., 2019). In contrast, all undrogued drifters are included to have enough segments since we focus on low, diurnal, semi-diurnal and near inertial frequenciesin Figure 3, as restricting the analysis to GPS-tracked drifters would lead to insufficient spatial coverage in parts of the domain (e.g., the equatorial South Atlantic; see Figure S1 in the supplementary).

The zonally averaged rotary spectra of OP Seed Drifters and undrogued drifters are shown in Figure **??**. Around the first row of Figure 3. Before contrasting the two datasets, we note that, near 30°N, the natural frequency of near-inertial oscillations (grey inertial frequency (grey dashed line) coincides with the diurnal tidal frequency (±1 cpd), making it difficult to disentangle their respective impactcontributions. This latitude corresponds to the so-called critical latitude , diurnal critical latitude (e.g., 27.6° for O_1 and 30° for K_1; Robertson (2001)), defined as the latitude where the inertial frequency equals the tidal frequency (e.g., Furevik and Foldvik, 1996; Middleton and Denniss, 1993; Robertson, 2001)(e.g., Middleton and Denniss, 1993; Robertson, 2001). According to linear internal wave theory, this it marks the poleward limit of wave propagation so, above poleward of 30°, diurnal internal tides become

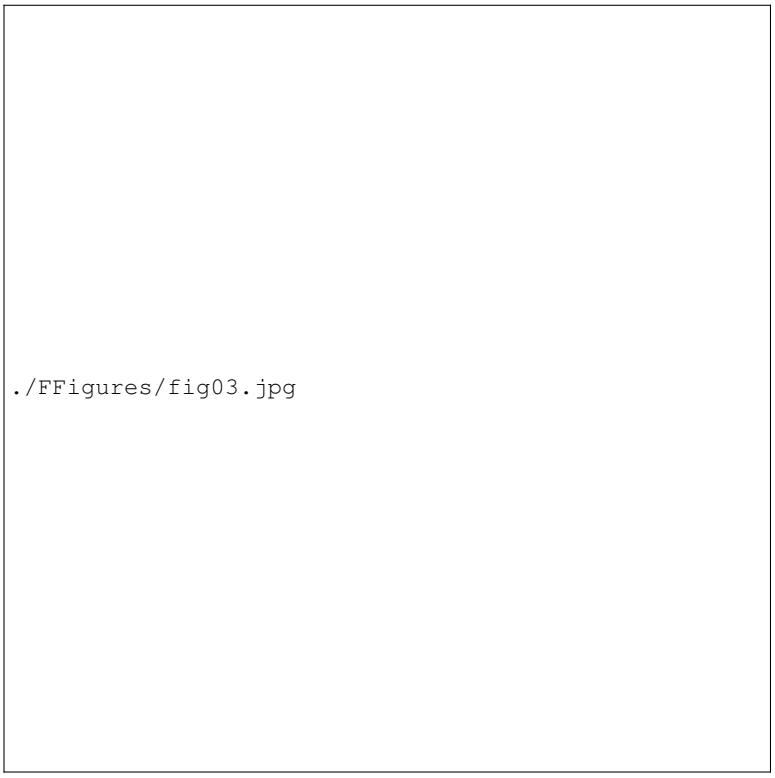

Figure 3. Zonally averaged rotary spectra in 1° latitude bins over regions in waters deeper than 500 m, in the NEATL domain for NEATL50-T-HB-HF computed from Ocean Parcel with a 1/2° seeding Comparison of OP Seed Drifters (a, first column) , from the and undrogued surface drifters (b, second column)and , with a normalized ratio obtained by dividing the first column by the sum of the first and second columns (c, last third column). A ; a ratio of 1/2 means that that the energies are indicates equal energies. Note The first row (a to c) shows the zonally averaged rotary spectra in 1° latitude bins computed over the offshore domain (waters deeper than 500 m) in the NEATL domain; note the decimal logarithmic color scale for panels a and b. The subsequent rows show maps of surface horizontal kinetic energy (SHKE) components over the first NEATL domain: low-frequency ($>$ -0.5 cpd and $<$ 0.5 cpd; second columnsrow, d to f); diurnal ($\pm$[0.9, 1.1] cpd; third row, g to i); semidiurnal ($\pm$[1.9, 2.1] cpd; fourth row, j to l); and near-inertial ($\pm$[0.9, 1.1]f cpd restricted poleward of $\pm 5^\circ$ latitude; fifth row, m to o). Note the decimal logarithmic color scale for all map panels.

Maps of kinetic energy (KE) components in the NEATL domain for NEATL50-T-HB-HF computed from Ocean Parcel with a 1/2° seeding (a, first column), from the undrogued drifters (b, second column) and a normalized ratio obtained by dividing the first column by the sum of the first and second columns (last column). Maps of low-frequency ($>$ -0.5 cpd and $<$ 0.5 cpd; first row, a to c); Maps of diurnal ($\pm$0.9, 1.1cpd; second row, d to f); Maps of semidiurnal ($\pm$1.9, 2.1cpd; third row, g to i) and Maps of near-inertial ($\pm$0.9, 1.1f cpd out of the band of latitude $\pm 5^\circ$ around the equator; fourth row, j to l). A ratio of 1/2 means that that the energies are equal. Note the decimal logarithmic color scale for all the panels.

325 evanescent. The critical latitude for low-frequency waves ($>$ -0.5 cpd and $<$ 0.5 cpd) lies near 15°, whereas for the semidiurnal ($\pm$2 cpd) band , it is much higher, around 75° , (e.g., 74.5° for M_2 and 85.7° for S_2; Furevik and Foldvik (1996); Robertson (2001)), allowing semidiurnal internal waves to propagate across most of the global ocean.

The pattern of the zonally averaged PSD of rotary spectra is similar between the observed and numerical drifters (Figure ??3a and b). However, the observed drifters show more energy in the high-frequency band, while the semidiurnal and diurnal peaks are, at most latitudinal bandslatitudes, more pronounced in the NEATL50-T-HB-HF numerical drifters. As discussed by Arbic et al. (2022), this high-frequency content in the observed drifters may originate from the drifter tracking system (Yu et al., 2019) and/or from artifacts in the estimation of drifter positions and velocities (Elipot et al., 2016). Overall, the numerical drifters contain less total energy SHKE than the observed undrogued surface drifters (Table ??2). Yet, they contribute to a significantly higher fraction to the low-frequency band, storing more that 8083.3% of the total energy (Table ??SHKE (87.8% of OP Seed 1/2°). In comparison, the undrogued drifters store 75.3% in the low-frequency band (64.3% for GPS-tracked drifters). In absolute and relative terms, the numerical particles exhibit more energy than observed in the semidiurnal and near-inertial bands. The difference in relative term is less marked for diurnal bands so the highest total energy in GPS-tracked drifters results in comparable diurnal-band energy levels for these observations than for numerical particles.

To assess regional differences, kinetic energy maps are presented in Figure **??**. Clear spatial contrasts emerge

The normalized ratio (right column in Figure 3) reveals clear spatial contrasts between the numerical simulation and the observations. At low frequencies, the model indicates higher KE in the center of the North Atlantic whereas the surface drifters show the opposite. In the semidiurnal and near-inertial bands, observations exhibit higher KE in energetic regions such as the Gulf of Mexico and the Gulf Stream, whereas the model distributes energy more broadly. Finally, in the diurnal band, Indeed, there is a striking bipolar pattern is found: observations show more KE poleward approximately 30°N, while the model shows more energy equatorward of this latitude. The bipolar pattern in the diurnal band , with more KE poleward of 30°N (Figure 3i) that is more pronounced in the observations but equatorward in the model, echoes the effect with higher SHKE poleward of the diurnal critical latitude : diurnal tides are evanescent poleward of around 30°N while near-inertial motions remain energetic there. By contrast, the absence of a comparable cutoff for semidiurnal tides allows them to propagate across the basin, which helps explain their more uniform and dominant imprint in the Eulerian simulations. Once can note that diurnal energy observed north of 30°N and less equatorward of it. This observed poleward diurnal energy is consistent with Arbic et al. (2022), which who reported that diurnal motions are driven not only by tides, but also by the day/night solar heating cycle.

In conclusion, the undrogued surface drifter data contains more total energy than numerical particles advected by the model velocity fields. When examining the distribution of energy across frequencies, both datasets show a comparable pattern. However, the model slightly over-represents the fraction of total energy in the At low frequencies, the model indicates higher SHKE in energetic regions such as the Gulf of Mexico and the Gulf Stream whereas the surface drifters show the opposite (Figure 3f). In the semidiurnal and near-inertial and semidiurnal reservoirs. Unexpected patterns emerge when scrutinizing the maps. In the bands, the pattern reverses, with observations exhibiting higher SHKE in these energetic regions, whereas the model distributes energy more broadly (Figure 3l and o). The effect of temporal coverage mismatch, resulting from the difference between the 30-year observational record and the single-year OP drifter simulation, is also weakly discernible in the near-inertial band specifically, spatial comparisons are hindered by the mismatch in temporal coverage: the observations span 30 years, while the OP drifters reflect variability from a single model year. For instanceband. Indeed, the two narrow bands of enhanced near-inertial energy between 20° and 30°N in panel j m of Figure ?? 3 for the 1-year numerical OceanParcels simulation correspond to the tracks of Hurricanes Fabian and Kate of the 2003 season , (the atmospheric forcing year of the model simulation(note that this feature simulation), a feature that is even more apparent in the Eulerian fields shown in panel j of Figure ??(Figure 4m).

Zonally averaged rotary spectra in 1° latitude bins over regions in waters deeper than $500\,m$, in the NEATL domain for OP Seed $1/2^\circ$ (a, first column), OP Seed drifters (b, second column) and a normalized ratio obtained by dividing the first column by the sum of the first and second columns (c, last column). A ratio of 1/2 means that that the energies are equal. Note the decimal logarithmic color scale for the first and second columns.

Maps of kinetic energy (KE) components in the NEATL domain for OP Seed $1/2^\circ$ (first column), OP Seed drifters (second column) and a normalized ratio obtained by dividing the first column by the sum of the first and second columns (last column). Maps of low-frequency ($>$ -0.5 cpd and $<$ 0.5 cpd; first row, a to c); Maps of diurnal ($\pm$0.9, 1.1cpd; second row, d to f); Maps of semidiurnal ($\pm$1.9, 2.1cpd; third row, g to i) and Maps of near-inertial ($\pm$0.9, 1.1f cpd out of the band of latitude $\pm 5^\circ$ around the equator; fourth row, j to l). A ratio of 1/2 means that that the energies are equal. Note the decimal logarithmic color scale for all the panels.

4.2 Impact of sampling

The above comparison to the observed drifter database was performed with the numerical drifters seeded uniformly on a $1/2^\circ \times 1/2^\circ$ grid for a total of 244,361 trajectory segments. This is a factor of 10 greater than Overall, the undrogued surface drifter data contains more total SHKE than NEATL50-T-HB-HF numerical particles, with the model over-representing the fraction of energy in the near-inertial and tidal reservoirs. Regionally, the sign of the model–observation discrepancy depends on the frequency band. At low frequencies, the modeled energy exceeds the observed one in the western boundary currents, whereas the reverse holds elsewhere. By contrast, in the semidiurnal and near-inertial bands, the observed energy exceeds the modeled one in these same energetic regions. The largest discrepancy is in the diurnal band. South of the diurnal critical latitude, where internal tides radiate freely, the number of segments (27,134) derived from the observed drifters. We therefore subsampled OP Seed $1/2^\circ$ to match the observed distribution (called OP Seed drifters) and compare the rotary spectra to quantify the impact of the number of drifters on the KE estimates. modeled diurnal energy exceeds the observed one while observations exceed the modeled one poleward, where only non-tidal mechanisms can sustain diurnal energy. Whether these discrepancies reflect genuine model biases or arise partly from the Lagrangian sampling framework is examined in the following subsection.

4.2 Lagrangian versus Eulerian sampling

When comparing the ratio of the zonally averaged PSD of rotary spectra from OP Seed The previous subsection established the differences between OP Seed Drifters and undrogued surface drifters. The effect of drifter sampling density on the 60-day segments and corresponding spectra was found to be small and spatially incoherent (see comparison between the high density OP Seed $1/2^\circ$ to OP Seed drifters (Figure **??**), we find no distinct spectral differences, apart from a frequency-independent positive bias in energy for the uniform OP Seed 1/2and subsampled OP Seed Drifters in Figure S2 and Section S3 of the supplementary). Restricting the undrogued drifter statistics to the OP Seed Drifters footprint (between 25°drifters. The exception is around 30S and 65°N where the ratio is near 0.5 which means the energies are nearly equal (Figure **??**c). This latitude bandcorresponds to the location of the North Atlantic gyre where , as shown in Figure 1c, the number of undrogued surface drifters is at a maximum. Thus, the KE level is impacted by the number of surface drifters, but, as shown in Tables **??** and **??**, it has a small impact on the KE averaged in our domain of studyN, not shown) yields nearly identical frequency distributions (to within 0.1 percentage points), with only a modest increase of total SHKE from 137.8 to 144.4×10^{-3} m^2 s^{-2}. This confirms that the spatial coverage of the OP experiments is not the main driver of the frequency-distribution mismatch between the model and the observations.

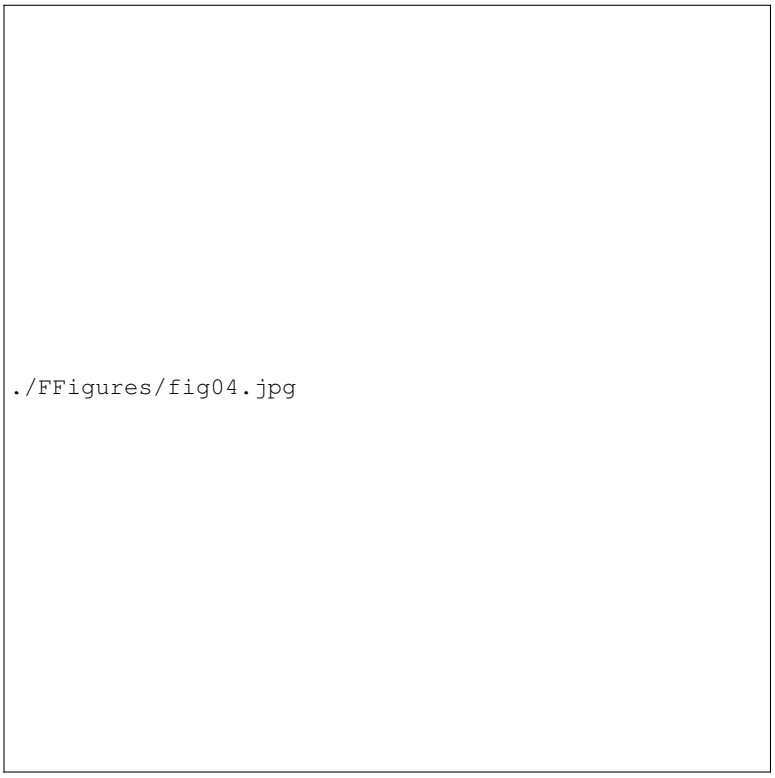

Figure 4. Zonally averaged rotary spectra in 1° latitude bins over regions in waters deeper than 500 m, in the NEATL domain for Comparison of NEATL50-T-HB-HF computed from Ocean Parcel (Lagrangian, a, first column) , from the original grid and OP Seed Drifters (Eulerian, b, second column)and , with a normalized ratio obtained by dividing the first column by the sum of the first and second columns (c, last third column). A ; a ratio of 1/2 means that that the energies are indicates equal energies. Note The first row (a to c) shows the zonally averaged rotary spectra in 1° latitude bins computed over the offshore domain (waters deeper than 500 m) in the NEATL domain; note the decimal logarithmic color scale for panels a and b. The subsequent rows show maps of surface horizontal kinetic energy (SHKE) components over the first NEATL domain: low-frequency ($>$ -0.5 cpd and $<$ 0.5 cpd; second columnsrow, d to f); diurnal ($\pm$[0.9, 1.1] cpd; third row, g to i); semidiurnal ($\pm$[1.9, 2.1] cpd; fourth row, j to l); and near-inertial ($\pm$[0.9, 1.1]f cpd restricted poleward of $\pm 5^\circ$ latitude; fifth row, m to o). Note the decimal logarithmic color scale for all map panels.

To assess the regional differences of OP seed vs. OP seed drifters, KE maps are presented in Figure **??**. As suggested by the zonal averaged studies, the energy level in the North Atlantic Gyre is similar at all the studied frequency bands. Otherwise, the uniform higher density of sampling results in more energy especially close to the coast where the number of available segments of undrogued surface drifters is the lowest (Figure 1c).

4.3 Lagrangian versus Eulerian sampling

Although surface drifters serve as the reference in this study, they are Lagrangian platforms, while the primary output from numerical simulations is Eulerian in nature. It is therefore crucial to assess the impact of using Lagrangian versus Eulerian velocities on the computation of the surface KE rotary spectra.

Maps of kinetic energy (KE) components in the NEATL domain for NEATL50-T-HB-HF computed from Ocean Parcel (Lagrangian, first column), from the original grid (Eulerian, second column) and a normalized ratio obtained by dividing the first column by the sum of the first and second columns (last column). Maps of low-frequency ($>$ -0.5 cpd and $<$ 0.5 cpd; first row, a to c); Maps of diurnal ($\pm$0.9, 1.1cpd; second row, d to f); Maps of semidiurnal ($\pm$1.9, 2.1cpd; third row, g to i) and Maps of near-inertial ($\pm$0.9, 1.1f cpd out of the band of latitude $\pm 5^\circ$ around the equator; fourth row, j to l). A ratio of 1/2 means that that the energies are equal. Note the decimal logarithmic color scale for all the panels.

The overall pattern is similar in the The zonally averaged PSD of rotary spectra calculated for NEATL50-T-HB-HF from is overall similar between the native Eulerian fields and in the Ocean Parcel Experiment (OP Seed 1/2°) OP Seed Drifters (Figure ??4a and b). However, the energy , but the tidal peaks are broader with respect to frequency in Lagrangian fields and disappear as the frequency increases. For example, the peaks around and increasingly indiscernible at higher frequencies in the Lagrangian spectra (e.g., the $\pm$4 cpd peaks are barely discernible in the Lagrangian spectra, whereas they are but prominent in the Eulerianspectra. This behavior, spreading of energy over broader frequency bands, is). This spectral broadening redistributes energy away from peak centers toward neighboring frequencies, as shown by the ratio in Figure 4c and consistent with observations from earlier work (Davis, 1983; Middleton, 1985; Zaron and Elipot, 2021; Caspar-Cohen et al., 2022; ?; Zhang et al., 2024). For frequencies close to these peaks, Lagrangian spectra generally exhibit higher energy as shown by the ratio in Figure ??c. The computation of domain-averaged energy stored (Davis, 1983; Middleton, 1985; Zaron and Elipot, 2021; Caspar-Cohen et al., 2022, 2025; Zhang et al., 2024). Above approximately $\pm$2.5 cpd, the Eulerian spectrum shows clear mirror images of the inertial ridge at $-f \pm 1$ cpd that appear as a surplus of Eulerian over Lagrangian energy (Figure 4c), while these features are barely discernible in the OP Seed Drifter (Figure 4b) and undrogued drifters spectra (Figure 3b). Their presence in our Eulerian fields corroborates the interpretation by Arbic et al. (2022), namely that such mirror images, previously identified in global surface drifters (Elipot et al., 2016) and in both Eulerian and Lagrangian global tide-resolving simulations (Zhang et al., 2024), reflect genuine oceanic processes. However, the attenuation of these mirror images in the Lagrangian spectrum suggests that the undrogued drifter sampling in the NEATL domain, although adequate for the frequency bands considered here, may under-resolve these weaker high-frequency features.

Domain-averaged energy in specific frequency reservoirs (absolute in Table ?? and relative in Table ??) show Tables 2 and S1) shows that the different velocities (Lagrangian vs. Eulerian) have minimal impact on total energy SHKE and in low, diurnal, and near-inertial bands, with maximum differences around 2%. However, significant deviations occur at higher frequency peaks, in the semidiurnal frequency band with Eulerian velocities containing up to 50% more energy in the semidiurnal frequency band than in than Lagrangian velocities. To assess the regional differences, KE maps in Figure ?? show that there is comparable level The SHKE maps (Figure 4) confirm comparable levels of energy for low, diurnal and near-inertial frequenciesin both datasets. For the semidiurnal frequencies, OP 1/12° has . In the semidiurnal band, OP Seed Drifters show less energy over most of the domain but that is not the case everywherewith a notable exception at the Amazon shelf (Figure 4j), a well-known hotspot of semidiurnal barotropic and internal tides (e.g., Gabioux et al., 2005; Beardsley et al., 1995; Tchilibou et al., 2022) where Lagrangian particles are advected across strong velocity gradients at each tidal cycle, likely amplifying the apparent tidal energy relative to Eulerian estimates.

The comparison of Lagrangian and Eulerian estimates (Figure 4) shows that the differences observed between OP Seed Drifters and undrogued surface drifters (Figure 3) cannot be attributed to the Lagrangian sampling alone. In particular, the Amazon Bank is associated with significantly more energy lower (higher) energy poleward (equatorward) of 30°N and the deficit

of high frequency energies in the model relative to observations are not visible when comparing OP Seed Drifters to the Eulerian fields, confirming that these are genuine dataset differences rather than an outcome of the Lagrangian sampling. Note that the high-frequency deficit in the simulations could partially be the result of drifter tracking and position-estimation artifacts (Elipot et al., 2016; Yu et al., 2019; Arbic et al., 2022) or wind slippage (Niiler and Paduan, 1995; Arbic et al., 2022) instead of real oceanic motions. Similarly, the higher observed SHKE in strong low-frequency flow, seen in the near-inertial and semidiurnal bands of the observation compared to the numerical drifters, is not recovered as a Lagrangian/Eulerian difference in our twin-simulation experiments. This contrasts with Zhang et al. (2024), who reported a Lagrangian underestimation of low-frequency and diurnal KE relative to the Eulerian field in regions of strong low-frequency flow. This apparent disagreement may be a consequence of a difference in experimental design as their analysis relied on a very large ensemble of particles distributed throughout the same simulation, providing the statistical power to isolate small Lagrangian sampling effects on energetic mesoscale regions. As in Zhang et al. (2024) and Caspar-Cohen et al. (2025), the main effect of the Lagrangian sampling is the spectral broadening of tidal peaks which has a negligible impact on the frequency distribution of low, diurnal and near-inertial bands (Table 2). In the semidiurnal band, however, the broadening is more pronounced, with the Eulerian fields storing 2.6% of total SHKE compared to 1.7% in the Lagrangian experiment, implying that part of any semidiurnal discrepancy between observations and Eulerian model output may reflect the Lagrangian/Eulerian framework itself.

5 Impact of model configuration and parameter choices on SHKE

The Lagrangian analysis yields three takeaways. First, numerical particles carry less total KE than Overall, the fact that the numerical simulations have less total SHKE than the observed undrogued drifters and that all also allocate a larger fraction of that energy to low frequencies , with relatively more energy in the semidiurnal and near-inertial bands. Second, samplingdensity has only a minor basin-scale influence. Third, Lagrangian estimates smooth tidal peaks and redistribute variance into the surrounding continuum, yielding substantially less semidiurnal energy than collocated Eulerian estimates. These results leads us to investigate the model parameters that are responsible for model–observation mismatches. We therefore turn to a (Table 2) is not a consequence of the drifters' Lagrangian sampling. There are, however, large differences in the other frequency bands among the numerical sensitivity experiments when compared to the observations and those are not uniform (Table 2). To quantify these differences, we analyze in detail the controlled series of sensitivity experiments that vary where a single model parameter at a time to quantify document the influence of resolution, tidal content, wind-forcing wind-forcing frequency, bathymetry, and wave drag, respectively.

5.1 Number of tidal components

The pattern of the zonally averaged PSD of rotary spectra calculated in the NEATL12-T and NEATL-12-M $_2$ experiments, which differ only in the number of tidal components forcing the model , is quite similar overall (eight largest tidal constituents and M_2 only, respectively). Their zonally averaged rotary spectra are broadly similar (Figure ??). However, with additional tidal constituents, 5a-c), but NEATL12-T has greater energy in the vicinity of the tidal peaks. This is particularly evident in the ratio plot normalized ratio (Figure ??5c), except at the exact position of the M_2 frequency (around ± 2 cpd) and its pure second harmonic (around ± 4 cpd, see Ray

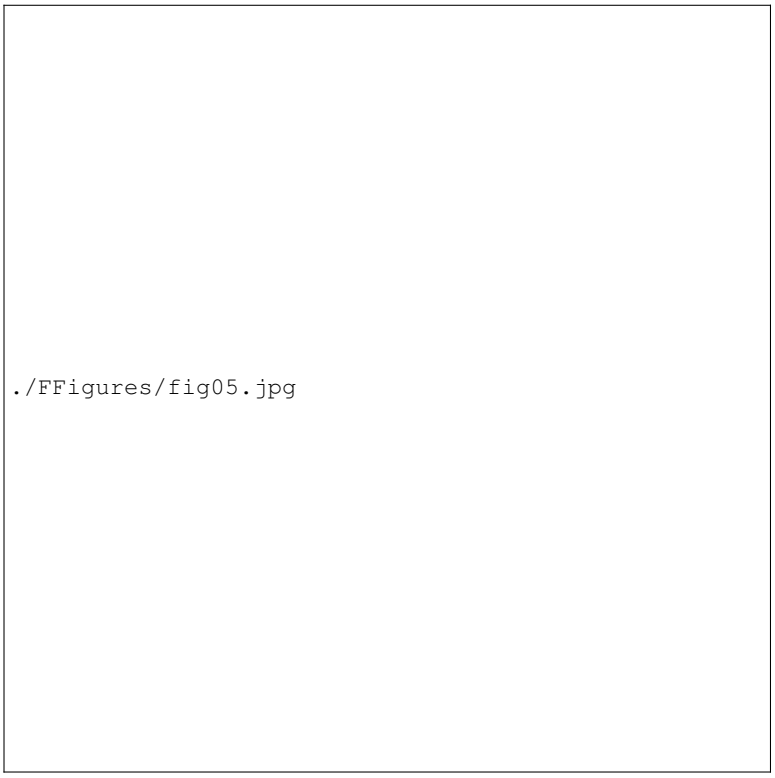

Figure 5. Zonally averaged rotary spectra in 1° latitude bins over regions in waters deeper than 500 m, in the NEATL domain for Comparison of NEATL12-T (a, first column) , and NEATL12-M_2 (b, second column)and , with a normalized ratio obtained by dividing the first column by the sum of the first and second columns (c, last third column). A ; a ratio of 1/2 means that that the energies are indicates equal energies. Note The first row (a to c) shows the zonally averaged rotary spectra in 1° latitude bins computed over the offshore domain (waters deeper than 500 m) in the NEATL domain; note the decimal logarithmic color scale for panels a and b. The subsequent rows show maps of surface horizontal kinetic energy (SHKE) components over the first NEATL domain: low-frequency ($>$ -0.5 cpd and $<$ 0.5 cpd; second columnsrow, d to f); diurnal ($\pm$[0.9, 1.1] cpd; third row, g to i); semidiurnal ($\pm$[1.9, 2.1] cpd; fourth row, j to l); and near-inertial ($\pm$[0.9, 1.1]f cpd restricted poleward of $\pm 5^\circ$ latitude; fifth row, m to o). Note the decimal logarithmic color scale for all map panels.

Maps of kinetic energy (KE) components in the NEATL domain for NEATL12-T (first column), NEATL12-M_2 (second column) and a normalized ratio obtained by dividing the first column by the sum of the first and second columns (last column). Maps of low-frequency ($>$ -0.5 cpd and $<$ 0.5 cpd; first row, a to c); Maps of diurnal ($\pm$0.9, 1.1cpd; second row, d to f); Maps of semidiurnal ($\pm$1.9, 2.1cpd; third row, g to i) and Maps of near-inertial ($\pm$0.9, 1.1f cpd out of the band of latitude $\pm 5^\circ$ around the equator; fourth row, j to l). A ratio of 1/2 means that that the energies are equal. Note the decimal logarithmic color scale for all the panels.

455 (2007)), where the tidal peak of NEATL-12-M $_2$ is comparable to that of NEATL12-T (i.e., normalized ratio near 0.5). Finally, at lower frequencies, the NEATL-12-M_2 simulation has comparable energy and, even at some specific latitudes in the anticyclonic side (i.e., positive frequencies), slightly more energy. Table **??** shows that reducing the number of tidal components slightly increases the total energy in the open ocean (i.e., averaged offshore KE of 96.810^{-3} $m^2\,s^{-2}$ in Figure 5c). Globally, the total SHKE remains essentially unchanged between the two runs (Table 2), with a slight decrease

offshore and a more notable increase on the shelf in NEATL12-T and of 98.110^{-3} m^2 s^{-2} in NEATL-12-M_2, see Table **??**). Conversely, NEATL12-T is more energetic on the continental shelf . The NEATL12-T. When fewer constituents are retained, the low-frequency component contains a slightly larger fraction of the total energy when fewer tidal components are considered SHKE (i.e., 91.8(% offshore and 45.7)% of offshore (inshore) total energy % inshore in NEATL12-T and against 92.4(% offshore and 48.7)% in NEATL-12-M% inshore in NEATL12-M_2, see Table **??**) , while , as expected to the results of zonally averaged PSD of rotary spectra, the diurnal, semidiurnal, and) while the near-inertial components bands contain a slightly smaller fraction.

To assess regional differences in KE reservoirs, KE maps over the NEATL domain are shown in Figure **??**. Regarding the energy stored in the low frequency band, no clear regional pattern emerges when the number of tidal components is increased (see Figure **??**a-c). To assess the regional differences in KE reservoirs, maps within the NEATL domain are presented in Figure **??**. Regarding the difference in energy stored at low frequencies, no clear regional difference is observed when the number of tidal components is increased (see Figure **??**a-c). One might notice more energy in There is also an increase in the NEATL-12-M_2 simulation (blue areas in Figure **??**c) in the Gulf of Mexico and near the Gulf Stream, areas known for rich mesoscale eddy activity (e.g., Chelton et al., 2011). In the diurnal band , semidiurnal fraction of total SHKE in NEATL12-T contains much more energy than compared to NEATL12-M_2 in the majority of the domain (see Figure **??**d-f). This is particularly true close to the coast (3 times more energy both in terms of absolute and percentage of total energy)as NEATL12-M_2 is the experiment with the lowest fraction of total energy stored in the diurnal band (Table **??**). Regions such as the Gulf of Mexico, western Caribbean, and Davis Strait, between Greenland and Canada, show much higher energy in the diurnal band associated with the presence of strong diurnal tides in those areas (Gouillon et al., 2010; Baumann et al., 2020). There are exceptions where both experiments have comparable energy, such as the North Atlantic gyre and in the Norwegian, Greenland, and Mediterranean seas, which correspond to the offshore regions at latitude higher than but the diurnal band concentrates the strongest contrast, with NEATL12-T more energetic both offshore and inshore but the largest differences are on the coast (a factor of three in both absolute and relative terms).

Regionally (Figure 5), no clear contrast between the two experiments emerges in the low-frequency, semidiurnal, and near-inertial bands with NEATL12-T being slightly more energetic in most of the domain. The diurnal band tells a different story with a clear separation at 30°(i.e., diurnal critical latitudes). It is worth noting that the high energy band south of the North Atlantic gyre (visible as a zonal band in Figure **??**d-e), around N. Poleward of 30°, is expected, as it corresponds to the latitude where near-inertial and diurnal frequencies overlap (Arbic et al., 2022; Raja et al., 2022). N the two experiments are comparable offshore, whereas equatorward of 30°N NEATL12-T contains slightly more energy in the semidiurnal band than NEATL12-M_2 (Figure **??**g-i). As shown in Figure **??**c, this is because the energy is distributed over a broader peak near ± 2 cpd in is significantly more energetic. On the shelves, the NEATL12-T than in NEATL12-M_2. One possible reason for this broader distribution is that the semidiurnal solar constituent S_2 is combined with M_2 in the NEATL12-T. Another possibility is that the first harmonic of the diurnal frequency is being added to the semidiurnal in NEATL12-T, but not in NEATL12-M_2, but, since there are no differences between open ocean and continental shelf regions, this is unlikely. The distribution and intensity of energy in the near-inertial frequency are very similar between the two experiments, with only small areas where either experiment contains more energyexcess of diurnal SHKE is present at all latitudes, including north of 30°N.

In conclusionOverall, adding more tidal components increases, as expected, the energy at the added peaks as one would expect. However, the impact is not homogeneous over the NEATL. Indeed, this is particularly marked frequencies, with the largest increase on the continental shelf, whereshelves where, through tidal shoaling, the barotropic tidal amplitudes are largest (Pugh and Woodworth, 2014). In the semidiurnal band, the slightly smaller fraction found in NEATL12-M_2 might reflect the absence of S_2, N_2, and K_2 constituents, which together contribute a non-negligible share of the global semidiurnal signal. Offshore and poleward of 30°N, the impact of the tides is the strongest. On the other hand, the experiment with fewer tidal components contains, on average, more energy at low frequencies. This is,

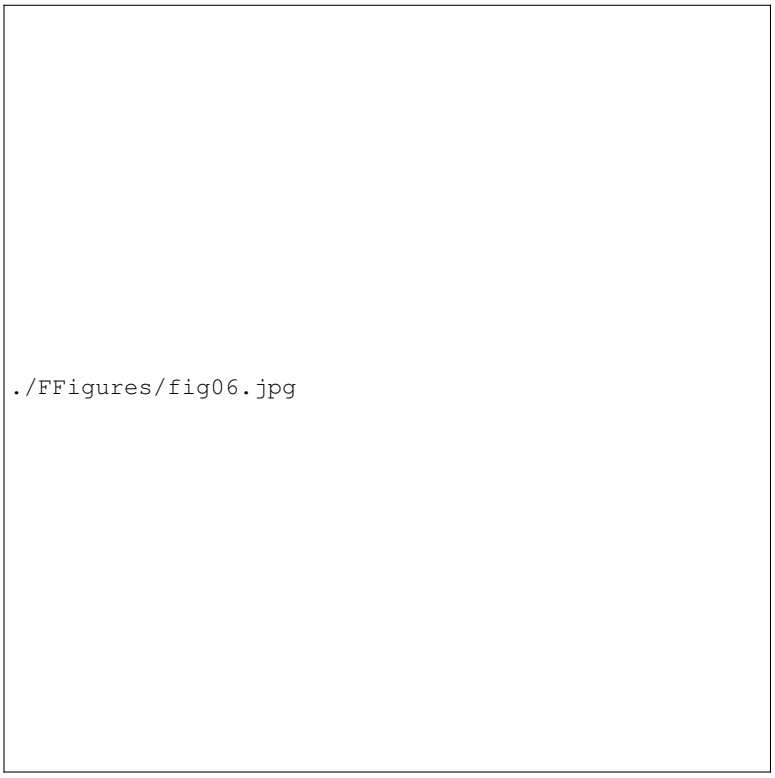

Figure 6. Zonally averaged rotary spectra in 1° latitude bins over regions in waters deeper than 500 m, in the NEATL domain for Comparison of NEATL50-T (a, first column) , and NEATL12-T (b, second column), and with a normalized ratio obtained by dividing the first column by the sum of the first and second columns (c, last third column). A ; a ratio of 1/2 means that that the energies are indicates equal energies. Note The first row (a to c) shows the zonally averaged rotary spectra in 1° latitude bins computed over the offshore domain (waters deeper than 500 m) in the NEATL domain; note the decimal logarithmic color scale for panels a and b. The subsequent rows show maps of surface horizontal kinetic energy (SHKE) components over the first NEATL domain: low-frequency ($>$ -0.5 cpd and $<$ 0.5 cpd; second columnsrow, d to f); diurnal ($\pm$[0.9, 1.1] cpd; third row, g to i); semidiurnal ($\pm$[1.9, 2.1] cpd; fourth row, j to l); and near-inertial ($\pm$[0.9, 1.1]f cpd restricted poleward of $\pm 5^\circ$ latitude; fifth row, m to o). Note the decimal logarithmic color scale for all map panels.

however, not uniform across the entire domain, as in some regions like the Labrador Sea, more energy is contained diurnal signal is nearly identical in both runs, highlighting that, as discussed by Arbic et al. (2022), a large fraction of the diurnal flow is non-tidal. Possible sources for this non-tidal diurnal SHKE are the wind variability (Dai and Deser, 1999; Savazzi et al., 2022; Dai, 2023) (further discussed in Section 5.6) and/or aliasing of mesoscale variability (Shriver et al., 2012; Buijsman et al., 2025). By contrast, the diurnal energy is substantially larger near the equator and on the shelves in NEATL12-T than in NEATL12-M_2, showing that the diurnal tidal constituents (K_1, O_1, P_1, Q_1) dominate the local diurnal variability in these regions.

5.2 Horizontal resolution

Maps of kinetic energy (KE) components in the NEATL domain for NEATL50-T (first column), NEATL12-T (second column) and a normalized ratio obtained by dividing the first column by the sum of the first and second columns (last column). Maps of low-frequency ($>$ -0.5 cpd and $<$ 0.5 cpd; first row, a to c); Maps of diurnal ($\pm$0.9, 1.1cpd; second row, d to f); Maps of semidiurnal ($\pm$1.9, 2.1cpd; third row, g to i) and Maps of near-inertial ($\pm$0.9, 1.1f cpd out of the band of latitude $\pm 5^\circ$ around the equator; fourth row, j to l). A ratio of 1/2 means that that the energies are equal. Note the decimal logarithmic color scale for all the panels.

Examining the zonally averaged PSD of rotating spectra calculated in the NEATL50-T and NEATL12-T experiments, which differ only in horizontal resolution (1/50° and 1/12°horizontal grid-spacing, respectively; Figure **??**), shows a clear contrast. The experiment with higher horizontal resolution (NEATL50-T) contains significantly more energy , respectively). The zonally averaged rotary spectra (Figure 6a-c) show that NEATL50-T is significantly more energetic at nearly all frequencies (see Figure 2 of Chassignet and Xu (2017) for a comparison of the time evolution of the domain-averaged total 3D kinetic energy - where 1/50° has approximately 70% more energy than 1/12°). This is confirmed by examining the ratio in Figure **??**6c and particularly true for frequencies whose absolute value exceeds 2 cycles per day. cpd. However, NEATL50-T is more energetic than and NEATL12-T at exactly $\pm$2 cpd, but the differences are small in the vicinity of these peaks have close levels of energy at tidal peaks close to $\pm$2 cpd. The only exception to the rule that higher resolution yields higher energy is that NEATL12-T has more energy in the near-inertial frequency bandnorth of 10°N.

Table **??** shows that the surface energy in the open $-[0.9, 1.1]f$ cpd frequency band, which corresponds to near-inertial motions in the northern hemisphere but to the cyclonic side of the spectrum in the southern hemisphere. Table 2 quantifies that the SHKE in the deep ocean increases by around one-third when the horizontal resolution increases from 1/12° to 1/50° horizontal grid-spacing; however, the differences are less pronounced on the continental shelf. The excess of energy is, roughly, well distributed across the different reservoirs, as the percentage of the total energy SHKE stored in each compartment is comparable between the two experiments(Table **??**). In detail, the most noticeable difference occurs in the open deep ocean where the percentage of total energy SHKE stored in the near-inertial band decreases by one-third (from 6% to 4%) as the resolution increases.

To assess the regional differences in details, maps are presented in Figure **??**. The Over most of the domain (Figure 6), the NEATL50-T simulation has significantly more energy than NEATL12-T at low, diurnal, and semidiurnal frequencies. However, the opposite is true for the near-inertial frequency. By contrast, near 30° latitude in the diurnal band, NEATL12-T has more energy than NEATL50-T, but this corresponds to the latitude where energy stored in the near-inertial band overlaps with that in the diurnal band (Arbic et al., 2022; Raja et al., 2022).

In conclusionOverall, increasing the horizontal resolution leads to a substantial increase in total energy SHKE across most of the energy spectrum, consistent with previous studies. Chassignet et al. (2020) showed that high horizontal-resolution simulations have much higher values of kinetic energy for low frequency motions compared to low-resolution simulations. For tidal frequencies, Buijsman et al. (2020) find that decreasing the horizontal grid-spacing found that increasing the horizontal resolution in realistic HYCOM simulations from 8 to 4 km increased the semidiurnal barotropic-to-baroclinic tidal conversion by 50%half, and more baroclinic modes were resolved, from 1-2 to 1-5 modes. Nelson et al. (2020) also found that decreasing the horizontal grid spacing , in this case in the regional Massachusetts Institute of Technology general circulation model (MITgcm) simulations, led leads to more realistic internal wave frequency spectra. The increase in horizontal resolution also leads to a better representation of the submesoscale field, and increases wave-mean and wave-wave interactions, thus explaining the increase in energy between peaks in wave–wave interactions, explaining the simulations with filling of the high-frequency continuum between the tidal peaks (Garrett and Munk, 1975) in the 1/50° horizontal

grid-spacing compared to those with simulations when compared to the 1/12° horizontal grid-spacing (Figure ??simulations (Figures 2 and 6c). The only exception is in There are two exceptions to this overall increase in SHKE. First, the semidiurnal fraction of the inshore SHKE decreases from 48.0% to 43.4% while the offshore fraction barely changes (1.9% to 2.0%; Table 2). A possible explanation is that over continental shelves, where the semidiurnal signal is predominantly barotropic and a large fraction of the global M_2 energy is dissipated (Egbert and Ray, 2001), enhanced barotropic-to-baroclinic conversion (Niwa and Hibiya, 2011; Buijsman et al., 2020) redistributes energy away from the barotropic tide, while the generated internal tide radiates seaward and is not retained locally. Yu et al. (2019) also suggested that insufficient horizontal resolution could enhance the semidiurnal peak by inhibiting scattering of tidal energy into the wave continuum (Müller et al., 2015; Shriver et al., 2012). Second, the near-inertial frequency band, where increasing the horizontal resolution results in a slight reduction of energy on average. Furthermore, even though the energy in the semidiurnal frequency band is close in the two simulations, the increase in total energy with higher resolution results in a markedly lower fraction of energy being associated with diurnal variability in the near-shore domain band is weaker on average at the higher horizontal resolution. One possible interpretation could be a more efficient vertical transport of near-inertial kinetic energy into the ocean interior through the resolved mesoscale and submesoscale fields in the 1/50° simulation (e.g., Kunze, 1985; Thomas et al., 2020; Lu et al., 2023). However, the spatial pattern in near inertial SHKE reduction does not straightforwardly support this view, since the reduction is not systematically concentrated in the most energetic regions of the domain (Figures 6d), where mesoscale activity is strongest, but rather appears in the basin interior.

5.3 Vertical resolution

Examining the zonally averaged rotating spectra calculated in the NEATL12-T-HVR and NEATL12-T experiments, which differ only in vertical resolution (32 and 96 vertical levels, respectively; Figure ??) , and 32 isopycnal layers, respectively). The zonally averaged rotary spectra (Figure 7a-b) show no clear differences emerge in either the total energy or the tidal peaks and in total SHKE, tidal peaks or harmonics. However, the ratio of the two normalized ratio indicates slightly more energy in the northern hemisphere high latitudes with more vertical levels (NEATL12-T-HVR) and less energy in the southern hemispherelow latitudes. As seen in Table ??2, increasing the vertical resolution from 32 to 96 levels results in a around approximately a 10 to 15% increase in total energySHKE, with the increase being higher over the continental shelf. This results in more energy in the different band-integrated KE components which is, as the Because the fraction of total energy does not change much SHKE in each band is largely unchanged (Table ??), distributed over 2), this additional energy is distributed broadly across the frequency domain. The most remarkable difference seen here is that, by increasing the vertical resolution, around 2% less of the total energy SHKE is stored in the near-inertial frequencies over the continental shelf.

To assess the regional differences in detail, kinetic energy maps are presented The maps in Figure ??. As with global integrals, the regional surface kinetic energy fields increase slightly with higher vertical resolution in the studied frequency ranges, particularly at low frequencies7 confirm the domain-averaged picture. Surface kinetic energy increases slightly across most regions and frequency bands when vertical resolution is refined, with no strong spatial pattern. The main exception lies offshore north of 40°N, where the differences can be substantial in some areas, such as the Gulf of Mexico. The increase in energy associated with higher vertical resolution is less pronounced for diurnal, semidiurnal, and near-inertial frequencies, although the increase is more uniform in the diurnal frequency band at the exception, again, of the 30°N latitudinal band. For high-frequency (supertidal)internal gravity waves, Nelson et al. (2020) finds increase appears spatially uniform in the diurnal band. This signal reflects the general increase of the

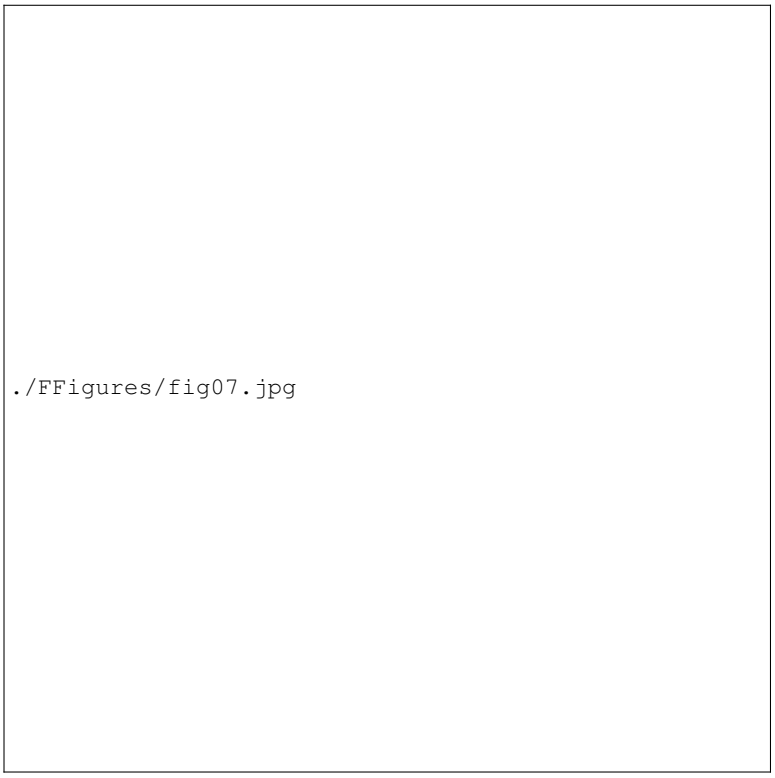

Figure 7. Zonally averaged rotary spectra in 1° latitude bins over regions in waters deeper than 500 m, in the NEATL domain for Comparison of NEATL12-T-HVR (a, first column) , and NEATL12-T (b, second column)and , with a normalized ratio obtained by dividing the first column by the sum of the first and second columns (c, last third column). A ; a ratio of 1/2 means that that the energies are indicates equal energies. Note The first row (a to c) shows the zonally averaged rotary spectra in 1° latitude bins computed over the offshore domain (waters deeper than 500 m) in the NEATL domain; note the decimal logarithmic color scale for panels a and b. The subsequent rows show maps of surface horizontal kinetic energy (SHKE) components over the first NEATL domain: low-frequency ($>$ -0.5 cpd and $<$ 0.5 cpd; second columnsrow, d to f); diurnal ($\pm$[0.9, 1.1] cpd; third row, g to i); semidiurnal ($\pm$[1.9, 2.1] cpd; fourth row, j to l); and near-inertial ($\pm$[0.9, 1.1]f cpd restricted poleward of $\pm 5^\circ$ latitude; fifth row, m to o). Note the decimal logarithmic color scale for all map panels.

Maps of kinetic energy (KE) components in the NEATL domain for NEATL12-T-HVR (first column), NEATL12-T (second column) and a normalized ratio obtained by dividing the first column by the sum of the first and second columns (last column). Maps of low-frequency ($>$ -0.5 cpd and $<$ 0.5 cpd; first row, a to c); Maps of diurnal ($\pm$0.9, 1.1cpd; second row, d to f); Maps of semidiurnal ($\pm$1.9, 2.1cpd; third row, g to i) and Maps of near-inertial ($\pm$0.9, 1.1f cpd out of the band of latitude $\pm 5^\circ$ around the equator; fourth row, j to l). A ratio of 1/2 means that that the energies are equal. Note the decimal logarithmic color scale for all the panels.

total SHKE, which stands out visually in this otherwise low-energy region, rather than a diurnal-specific enhancement. Another exception regards regions of intense mesoscale activity, with elevated low-frequency energy in the corridors of North Brazil Current rings (Fratantoni and Glickson, 2002), Gulf of Mexico Loop Current eddies (Leben, 2005), and Gulf

Stream meanders/rings, largely masked by the high background energy in the ratio panel (Figure 7f), but evident when comparing the pathways in panels d and e.

Overall, vertical refinement increases the total SHKE, distributed broadly across the frequency domain (see also Figure 2), with a coherent enhancement at high latitudes. This is consistent with various studies that show that tidal energetics vary with the number of vertical layers provided that horizontal grid spacing is not the limiting factor. Nelson et al. (2020) showed that the modeled internal wave frequency spectra is are improved with increased vertical resolution only when the horizontal resolution is also increased. In an idealized 1/100° HYCOM configuration forced solely by semidiurnal tides, Hiron et al. (2025) find found that increasing the number of isopycnal layers increases tidal-induced vertical velocities and available potential energy, while tidal kinetic energy remains largely unchanged. The energetics increase up to 48 layers and change little thereafter. These studies show that tidal energetics among simulations with different number of layers vary as long as horizontal grid-spacing is not limiting. Here, for Here, at 1/12° horizontal grid-spacing, the minimal changes in semidiurnal energy between the simulation with tidal SHKE changes only weakly between 32 and 96 layersmight suggest , and the tidal SHKE fraction even decreases slightly, suggesting that the horizontal grid-spacing is limiting, or that kinetic energy in the semidiurnal frequency is not significantly impacted by changes in vertical number of layers.

In conclusion, increasing the vertical resolution results in a increase in energy which is distributed over the frequency domain (see also Figure 2)the limiting factor in our configuration. The dominant effect of vertical refinement is therefore an increase of low-frequency SHKE, also visible in total KE (not shown), in the already energetic meso- and large-scale flow regions, consistent with the primary role of the vertical grid in resolving horizontal flows via improved representation of their baroclinic structure (Stewart et al., 2017; Xu et al., 2023).

5.4 Impact of topographic internal wave drag

Zonally averaged rotary spectra from the NEATL50-T-WD and NEATL50-T experiments, which differ only by differ only in the inclusion of wave drag internal wave drag (Jayne and St. Laurent, 2001) in NEATL50-T-WD, are shown in Figure ??. The addition . The zonally averaged rotary spectra (Figure 8) show that the inclusion of wave drag results in a reduction of reduces energy across the majority of the frequency domain. The differences are less pronounced in frequencies lower than reduction is less pronounced at frequencies below the near-inertial frequency, where the differences are band, where it becomes almost negligible. Table ?? 2 confirms that the inclusion of wave drag leads to a slight decrease in energy across all the frequency bands analyzed. The most significant impact is observed pronounced impact is in the semidiurnal frequency within the offshore domainband, where the addition of wave drag results in an energy reduction of approximately 25% , while differences, although present, are less pronounced inshore . fraction of total SHKE drops by about 0.4-0.5% both inshore (from 43.4% to 42.9%) and offshore (from 2.0% to 1.6%). While this represents a small relative change inshore, offshore it corresponds to a relative reduction of about 1/5.

To assess regional variations, KE maps are displayed in Figure ??. These maps confirms The SHKE maps (Figure 8) confirm that incorporating wave drag leads to a overall reduced surface KE an overall reduction in surface SHKE across the frequency bands studied. In the low-frequency band, a clear reduction is visible in the tropical band equatorward of around $\pm 15°$ (Figure 8d-f). In the diurnal band, the reduction is most apparent equatorward of 30°N, while no clear signal emerges poleward of this latitude, where diurnal tides become evanescent. In contrast, the decline in semidiurnal energy is more pronounced in the open deep ocean at nearly

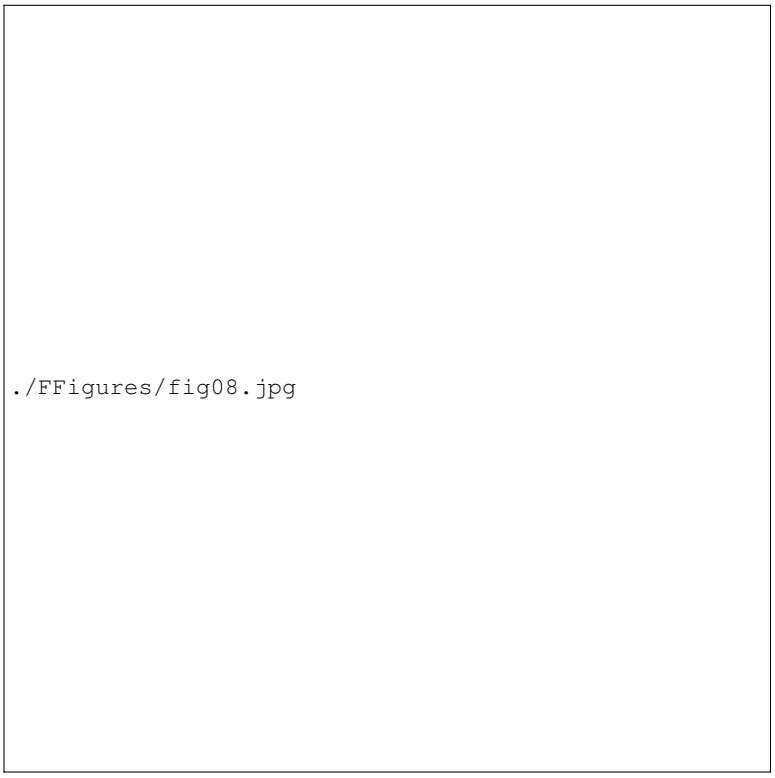

Figure 8. Zonally averaged rotary spectra in 1° latitude bins over regions in waters deeper than 500 m, in the NEATL domain for Comparison of NEATL50-T-WD (a, first column) , and NEATL50-T (b, second column)and , with a normalized ratio obtained by dividing the first column by the sum of the first and second columns (c, last third column). A ; a ratio of 1/2 means that that the energies are indicates equal energies. Note The first row (a to c) shows the zonally averaged rotary spectra in 1° latitude bins computed over the offshore domain (waters deeper than 500 m) in the NEATL domain; note the decimal logarithmic color scale for panels a and b. The subsequent rows show maps of surface horizontal kinetic energy (SHKE) components over the first NEATL domain: low-frequency ($>$ -0.5 cpd and $<$ 0.5 cpd; second columnsrow, d to f); diurnal ($\pm$[0.9, 1.1] cpd; third row, g to i); semidiurnal ($\pm$[1.9, 2.1] cpd; fourth row, j to l); and near-inertial ($\pm$[0.9, 1.1]f cpd restricted poleward of $\pm 5^\circ$ latitude; fifth row, m to o). Note the decimal logarithmic color scale for all map panels.

Maps of kinetic energy (KE) components in the NEATL domain for NEATL50-T-WD (first column), NEATL50-T (second column) and a normalized ratio obtained by dividing the first column by the sum of the first and second columns (last column). Maps of low-frequency ($>$ -0.5 cpd and $<$ 0.5 cpd; first row, a to c); Maps of diurnal ($\pm$0.9, 1.1cpd; second row, d to f); Maps of semidiurnal ($\pm$1.9, 2.1cpd; third row, g to i) and Maps of near-inertial ($\pm$0.9, 1.1f cpd out of the band of latitude $\pm 5^\circ$ around the equator; fourth row, j to l). A ratio of 1/2 means that that the energies are equal. Note the decimal logarithmic color scale for all the panels.

all latitudes, with the exception of the western boundary current pathway from the Gulf of Mexico into the Gulf Stream (Figure 8j-l). Finally, in the near-inertial band, no clear signal emerges.

In conclusionOverall, the inclusion of wave drag results in reduced energy in the frequency bands located below their respective critical latitudes reduces the energy in each frequency band over the latitudes where the corresponding motions can propagate, that is, around

equatorward of about ±15° for the low-frequency band (below ± 0.5 cpd), ±30° for the diurnal band, and almost across nearly the entire domain for the semidiurnal band, except along the western boundary current pathway. By construction, wave drag primarily affects propagating tidesand this energy reduction is to be expecteddissipates propagating tides, which explains the absence of a clear difference poleward of these critical latitudes, where the motions become evanescent. Yu et al. (2019) reported that the MITgcm tends to overestimate semidiurnal SHKE compared to surface drifters and, following Arbic et al. (2010) and Ansong et al. (2015), attributed this bias partly to the absence of topographic internal wave drag in the MITgcm simulations. Our results support this interpretation, with lower semidiurnal energy when wave drag is included. Moreover, the observed latitudinal pattern confirms that the inclusion of wave drag enhances barotropic tidal dissipation, consistent with the findings of Buijsman et al. (2015).

5.5 Bathymetry resolution

Chassignet et al. (2003) showed that the inclusion of high-resolution bathymetry can lead to a significant impact on the Gulf Stream pathway and variability. The NEATL50-T-HB and NEATL50-T experiments differ only by the higher resolution of the bathymetry in differ only in bathymetric resolution, with NEATL50-T-HB (see Chassignet et al. (2023) for details)using a native 1/50° bathymetry rather than the 1/12° product interpolated onto the 1/50° grid (Chassignet et al., 2023). Overall, increasing the bathymetry resolution leads to a reduction in energy in the higher-resolution bathymetry reduces the SHKE across most of the frequency domain (Figure **??**). However, notable exceptions are see Figure 9a-c and Table 2). There are, however, notable exceptions in the semidiurnal and higher-frequency tidal peaks , and and in the latitudinal band between 20°N and 30°N, where the SHKE is higher in the high-resolution bathymetry simulation. Table **??** confirms that the total energy decreases when the bathymetry resolution is increased from 1/12° to 1/50°. In the open ocean, the distribution between high and low frequencies remains consistent (Table **??**). However, The low-frequency fraction of SHKE is only marginally reduced (from 92.2% to 91.4%), whereas in shallow regions , a slight reduction in energy transfer to low frequencies is observed—accounting for 45% rather than the previous it drops more noticeably, from 49.7% to 45.0% (Table 2). There are minimal changes in the diurnal and near-inertial components, but enhancing the bathymetry resolution leads to an increased energy in the semidiurnal frequency band. The percentage of KE contained in the semidiurnal band increased from 2% to 2.543.4% to 48.0% in the shelf domain, and from 43.4% to 48.12.0% to 2.5% in the offshore domain when high-resolution bathymetry was used.

To assess the regional differences, KE maps are presented in Figure **??**. Examining the KE maps The SHKE maps (Figure **??**) , we find that the increase in bathymetry resolution does not have a clear impact on the energy for 9) do not show clear regional differences in the low-frequency and near-inertial bands, as both patches of higher and lower frequency are present. This could indicate, as examined for the Gulf Stream by Chassignet and Xu (2021) and Chassignet et al. (2023), a change in circulation patterns rather than a direct impact on the energy itself. With . A noteworthy exception is the enhancement (diminution) of low-frequency SHKE below (above) the equator off the the Amazon shelf (Figure 9f). In the diurnal frequency bandWith, there is a reduction of energy in the higher-resolution bathymetry experiment, with the exception of the 30°N latitude and a few specific regions such as the Adriatic Sea, the higher-resolution bathymetry tends to reduce energy in the diurnal frequency band. In . By contrast, in the semidiurnal band, the increase in bathymetry resolution increases the surface SHKE , with a few exceptions, mainly at high latitudes. There is also a clear increase in the SHKE associated with semidiurnal internal tides in the Amazon Shelf. A higher-resolution bathymetry product resolves more topographic gradients, leading to higher barotropic-to-baroclinic tidal conversion, and subsequent increase in semidiurnal tides KE, in agreement with Xu et al. (2022). shelf.

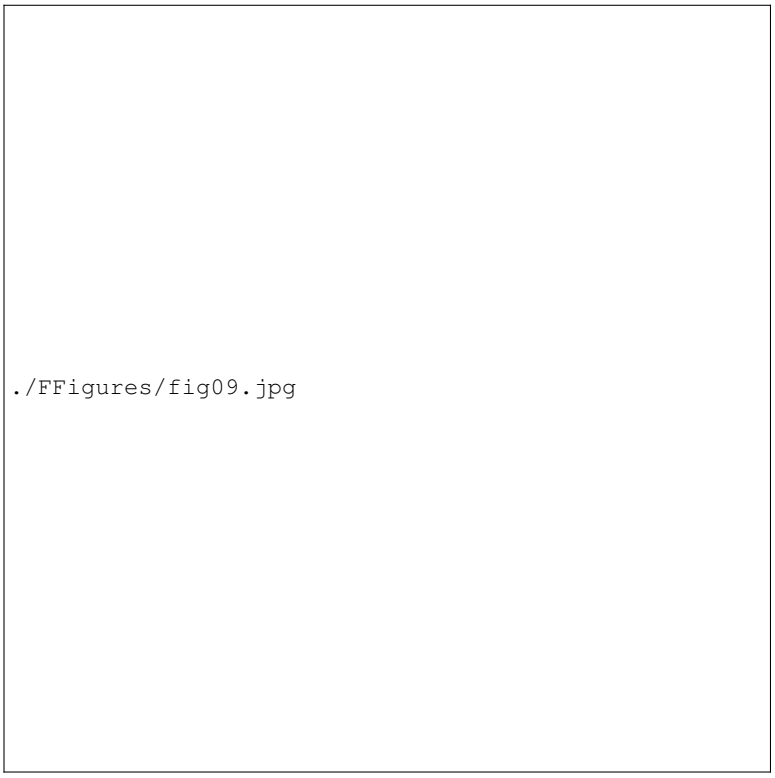

Figure 9. Zonally averaged rotary spectra in 1° latitude bins over regions in waters deeper than 500 m, in the NEATL domain for Comparison of NEATL50-T-HB (a, first column) , and NEATL50-T (b, second column)and , with a normalized ratio obtained by dividing the first column by the sum of the first and second columns (c, last third column). A ; a ratio of 1/2 means that that the energies are indicates equal energies. Note The first row (a to c) shows the zonally averaged rotary spectra in 1° latitude bins computed over the offshore domain (waters deeper than 500 m) in the NEATL domain; note the decimal logarithmic color scale for panels a and b. The subsequent rows show maps of surface horizontal kinetic energy (SHKE) components over the first NEATL domain: low-frequency ($>$ -0.5 cpd and $<$ 0.5 cpd; second columnsrow, d to f); diurnal ($\pm$[0.9, 1.1] cpd; third row, g to i); semidiurnal ($\pm$[1.9, 2.1] cpd; fourth row, j to l); and near-inertial ($\pm$[0.9, 1.1]f cpd restricted poleward of $\pm 5^\circ$ latitude; fifth row, m to o). Note the decimal logarithmic color scale for all map panels.

Maps of kinetic energy (KE) components in the NEATL domain for NEATL50-T-HB (first column), NEATL50-T (second column) and a normalized ratio obtained by dividing the first column by the sum of the first and second columns (last column). Maps of low-frequency ($>$ -0.5 cpd and $<$ 0.5 cpd; second row, a to c); Maps of diurnal ($\pm$0.9, 1.1cpd; third row, d to f); Maps of semidiurnal ($\pm$1.9, 2.1cpd; third row, g to i) and Maps of near-inertial ($\pm$0.9, 1.1f cpd out of the band of latitude $\pm 5^\circ$ around the equator; third row, j to l). A ratio of 1/2 means that that the energies are equal. Note the decimal logarithmic color scale for all the panels.

In conclusion, increasing the bathymetry resolutionslightly decreases the energy and, as discussed by Chassignet and Xu (2021) and Chassignet et al. (2023), can lead to changes in large-scale circulation patterns, as indicated by both local increases or decreases of KE for The reduction in the total SHKE of NEATL50-T-HB when compared to NEATL50-T is consistent with the enhanced lateral and bottom dissipation due to the increase in bathymetric resolution (Zhai et al., 2010; Ferrari and Wunsch, 2009), both of which are more accurately represented in

the finer bathymetric resolution. This reduction is achieved through a transfer of energy toward higher-frequency motions via flow–topography interactions and internal wave generation (e.g., Ferrari and Wunsch, 2009; Nikurashin and Ferrari, 2010; De Marez et al., 2020). This mechanism is consistent with the observed reduction of low-frequency motions. The increase SHKE, which occurs in both subdomains, but it is much more pronounced on the continental shelf than in the deep ocean, likely reflecting the enhanced coupling between surface and bottom processes in shallow waters, where the bottom is closer to the surface and more directly shapes the surface kinetic energy. However, changes are spatially heterogeneous, with local increases and decreases in bathymetry resolution also low-frequency energy, in agreement with bathymetry-induced modifications of the large-scale circulation (Chassignet and Xu, 2021; Chassignet et al., 2023) as, for example, on the Amazon shelf near the North Brazil Current retroflection. In the semidiurnal band, there is an energy increase almost everywhere and we surmise this is due to a better representation of local internal wave generation with better-resolved bathymetry (Xu et al., 2022). This is supported by the more pronounced signature observed over the Amazon shelf (Figure 9i), consistent with the strong M_2 barotropic-to-baroclinic conversion documented in that region (Beardsley et al., 1995; Tchilibou et al., 2022). In contrast, the higher bathymetry resolution tends to reduce the energy of the diurnal peak, but increase that for the semidiurnal peak and tidal peaks at higher frequenciesdiurnal energy, especially equatorward of its critical latitude, possibly reflecting enhanced dissipation of propagating internal waves.

5.6 Temporal frequency of atmospheric forcing

Table ?? compares NEATL50-T-HB-HF and NEATL50-T-HB experiments, which differ only in the temporal frequency of the wind forcing(higher in , with NEATL50-T-HB-HF)using hourly wind stress rather than 6-hourly. Increasing the wind-forcing frequency leads to an overall rise in surface KE a rise in SHKE across all frequency bands . The increase is seen in both the open ocean and on the continental shelf(Table S1 in the supplementary). However, this increase is not uniformdoes not necessarily imply an increase in all bands when when expressed as fractions of total SHKE (Table 2). For example, there is a reduced fraction of total to percentage in the low frequencies in the offshore domain (86.7% instead of 91.4%) while it remains comparable close to the coasts inshore (44.8% instead of 45.0%) (Table ??). 2). The near-inertial band on the shelf shows almost no net change in total SHKE (Table S1 in the supplementary), because the overall increase of total SHKE is compensated by a reduction in the near-inertial fraction at higher temporal frequency (Table 2). At high frequencies, the energy in the diurnal and band (offshore and inshore) and in the offshore near-inertial bandsshows a large increase, by more than 50%. This is also visible in Figure ?? 10a-c where zonally averaged rotary spectra are compared. We find that an increase in wind frequency increases the energy in nearly all the frequency domains at all latitudes, with the exception of low and semidiurnal frequency motions where the level of energy is comparable. While there is also an increase on the shelf in the near-inertial band (Table **??**), it is considerably less pronounced and comparable to the total increase of energy (Table **??**).

To assess the regional differences, KE maps are presented in Figure **??**. Examining these maps, we find that the domain-averaged increase in Spatially, the increase in energy for higher wind frequency is not evenly distributed, as in some regions, higher temporal frequency of wind results in less energy. There is a clear increase of energy for both mostly uniform for the low frequency, diurnal and near-inertial frequency bands (Figure 10). However, in the middle of the Atlantic, there is no large signal on the KE in the semidiurnal frequency band, but higher wind frequency leads to significantly higher semidiurnal KE in closed

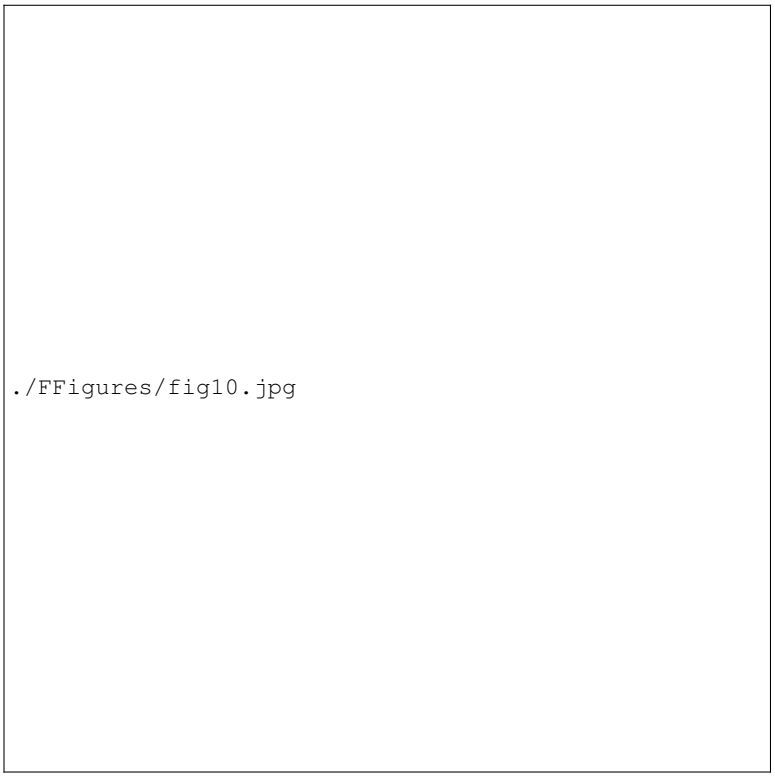

Figure 10. Zonally averaged rotary spectra in 1° latitude bins over regions in waters deeper than 500 m, in the NEATL domain for Comparison of NEATL50-T-HB-HF (a, first column) , and NEATL50-T-HB (b, second column)and , with a normalized ratio obtained by dividing the first column by the sum of the first and second columns (c, last third column). A ; a ratio of 1/2 means that that the energies are indicates equal energies. Note The first row (a to c) shows the zonally averaged rotary spectra in 1° latitude bins computed over the offshore domain (waters deeper than 500 m) in the NEATL domain; note the decimal logarithmic color scale for panels a and b. The subsequent rows show maps of surface horizontal kinetic energy (SHKE) components over the first NEATL domain: low-frequency ($>$ -0.5 cpd and $<$ 0.5 cpd; second columnsrow, d to f); diurnal ($\pm$[0.9, 1.1] cpd; third row, g to i); semidiurnal ($\pm$[1.9, 2.1] cpd; fourth row, j to l); and near-inertial ($\pm$[0.9, 1.1]f cpd restricted poleward of $\pm 5^{\circ}$ latitude; fifth row, m to o). Note the decimal logarithmic color scale for all map panels.

Maps of kinetic energy (KE) components in the NEATL domain for NEATL50-T-HB-HF (first column), NEATL50-T-HB (second column) and a normalized ratio obtained by dividing the first column by the sum of the first and second columns (last column). Maps of low-frequency ($>$ -0.5 cpd and $<$ 0.5 cpd; first row, a to c); Maps of diurnal ($\pm$0.9, 1.1cpd; second row, d to f); Maps of semidiurnal ($\pm$1.9, 2.1cpd; third row, g to i) and Maps of near-inertial ($\pm$0.9, 1.1f cpd out of the band of latitude $\pm 5^{\circ}$ around the equator; fourth row, j to l). A ratio of 1/2 means that that the energies are equal. Note the decimal logarithmic color scale for all the panels.

seas such as the increase is only confined to specific regions, e.g, the Gulf of Mexico, Mediterranean Sea, Baltic Sea, Norwegian
680 Sea and Greenland Sea.

In conclusion, increasing the frequency of wind forcing increases the total KE and at high frequency Overall, the increase in wind forcing frequency raises the total SHKE across most of the domain . The large increase of KE for diurnal (3 times in off-shore) and through a gain of high-

frequency energy. A strong amplification occurs in the near-inertial (nearly 2 times in off-shore) is expected as winds have a diurnal cycle and winds are one of the main sources of band, consistent with the known role of the wind in driving near-inertial motions (Klein et al., 2004; Rimac et al., 2013). However, as noted by Rimac et al. (2013) and Yu et al. (2019), the impact of increasing the wind frequency on (Klein et al., 2004; Rimac et al., 2013; Flexas et al., 2019). As noted by several authors (Rimac et al., 2013; Yu et al., 2019; Raja et al., 2022), this near-inertial motions response is less pronounced in tropical and subtropical regions than in at mid-latitudes (lower right panel of Figure **??**). There is also a marked increase of semidiurnal energy in closed sea. Figure 10o). A more unexpected feature is the strong amplification in the diurnal band almost everywhere and in the semidiurnal band in regions of weak semidiurnal energy such as semi-enclosed basins. This behavior likely reflects the diurnal and semidiurnal cycles of the wind itself (Dai and Deser, 1999; Savazzi et al., 2022; Dai, 2023). In particular, Dai and Deser (1999) estimated globally that the diurnal cycle accounts for 30–40% of the daily wind variance over the ocean, whereas the semidiurnal cycle accounts for only 15–25%. The dominant diurnal share explains why the wind-forced signal covers most of the domain in the diurnal band. The semidiurnal share, by contrast, is small enough that the directly wind-forced response can only emerge clearly where the background astronomical semidiurnal tide is itself weak, which is precisely the case in the semi-enclosed basins where we observe the amplification in the ratio maps. Consistently, no such amplification appears in regions known for resonant astronomical semidiurnal tides, such as the North Sea (e.g., Jänicke et al., 2021), the English Channel and Irish Sea (e.g., Webb, 2013), Hudson Bay (e.g., Cummins et al., 2010), and the Bay of Fundy–Gulf of Maine system (e.g., Garrett, 1972), where the strong astronomical signal is expected to mask the wind-forced response. Note that the diurnal amplification appears weaker near 30° in Figure 10i.

In this paper, we investigated surface kinetic energy (KE) distributions in the North and Equatorial Atlantic (NEATL) using seven tide-resolving HYCOM experiments, one numerical Lagrangian simulation (Ocean Parcels, OP), and observations from surface drifters. For each comparison, we considered both absolute KE values and the fraction of total KE contained in different frequency bands. The latter isolates changes in spectral distribution from changes in overall energy ; accordingly, all reported band percentages are fractions of total KE. The analysis proceeded in three steps.

6 Summary and conclusion

First, a domain-wide comparison of rotary spectra from all datasets established the large-scale spectral structure and highlighted systematic differences between models and observations. All spectra showed the expected low-frequency dominance (Wunsch and Stammer, 1995; Ferrari and Wunsch, 2009; Morrow and Le Traon, 2012) and distinct tidal and near-inertial peaks, with horizontal resolution emerging as the main distinction between all simulations: the KE in

The experimental suite analyzed in the previous section allows us to attribute changes in total surface horizontal kinetic energy (SHKE) and its frequency distribution to individual numerical choices (grid and bathymetry resolution, wind and tidal forcing, and wave drag). In this section, we discuss the parameters that most strongly affect the SHKE distribution in each frequency band and, where applicable, how they could be adjusted to reduce the model-drifter gap. Figure 11 synthesizes, for each of the 1/50° numerical simulations were systematically closer to that of the observed drifters than the 1/12° simulations. The six sensitivity experiments, the relative change in total and per-band SHKE for the offshore ($> 500\,\mathrm{m}$) and continental-shelf ($< 500\,\mathrm{m}$)

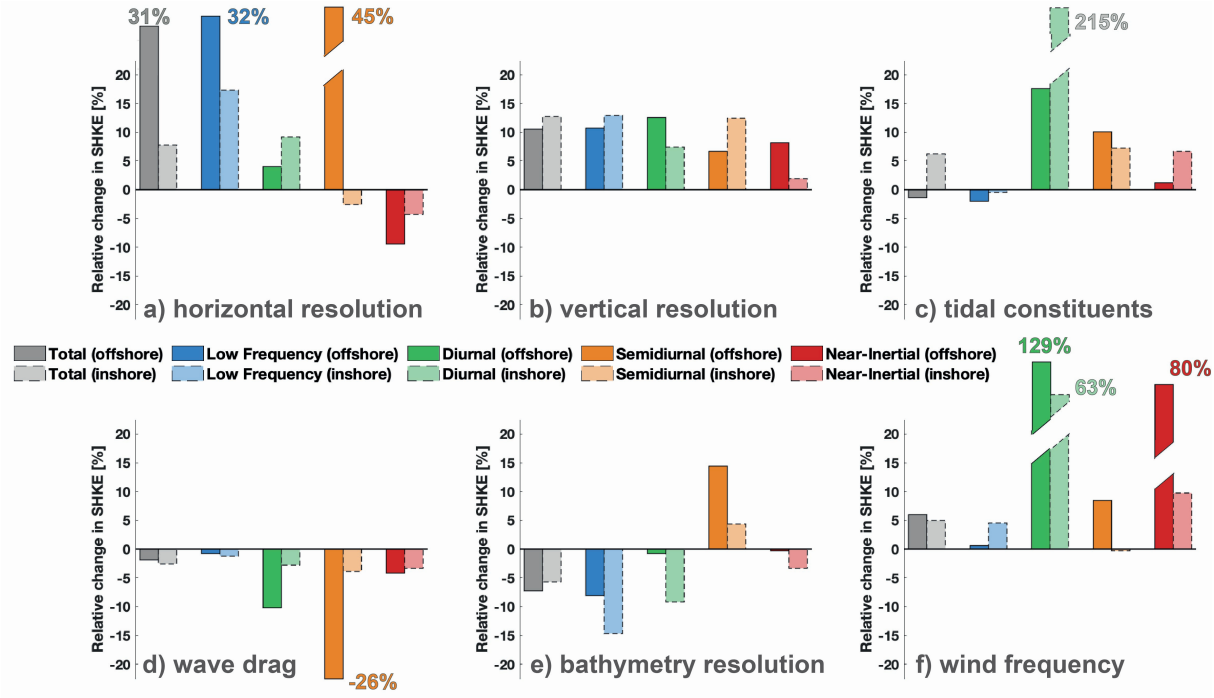

Figure 11. Sensitivity of the domain-averaged surface horizontal kinetic energy (SHKE) to six model configuration choices, separately for the offshore (waters deeper than 500 m; filled bars, solid edges) and continental shelf (waters shallower than 500 m; lighter bars, dashed edges) subdomains of the NEATL region. Each panel shows the relative change in SHKE, $(\mathrm{SHKE_{mod}} - \mathrm{SHKE_{ctrl}})/\mathrm{SHKE_{ctrl}}$ (in %), induced by a single parameter modification, decomposed into five components: total SHKE (grey), low-frequency ($>$ -0.5 cpd and $<$ 0.5 cpd, blue), diurnal ($\pm$[0.9, 1.1] cpd, green), semidiurnal ($\pm$[1.9, 2.1] cpd, orange), and near-inertial ($\pm$[0.9, 1.1]f cpd restricted poleward of $\pm 5^\circ$ latitude, red). The six parameter pairs (control to modified) are: (a) horizontal resolution, NEATL12-T to NEATL50-T; (b) vertical resolution, NEATL12-T to NEATL12-T-HVR; (c) number of tidal constituents, NEATL12-M_2 to NEATL12-T; (d) inclusion of internal wave drag, NEATL50-T to NEATL50-T-WD; (e) bathymetry resolution, NEATL50-T to NEATL50-T-HB; (f) atmospheric forcing temporal frequency, NEATL50-T-HB to NEATL50-T-HB-HF. The vertical axis is clipped at $\pm$20% for readability; values outside this range are reported numerically above (positive) or below (negative) the corresponding bar.

regions. This forms the backbone of the discussion that follows where each of the next paragraphs focuses on one frequency band.

The total SHKE (grey in Figure 11) is most sensitive to horizontal resolution in the offshore region, where refining the horizontal grid from $1/12^\circ$ to $1/50^\circ$ increases the offshore SHKE by about one third (+31%, Figure 11a). The increase in horizontal resolution is also the parameter that fills the most the high-frequency continuum between tidal peaks, i.e., the so-called Garrett–Munk spectrum (Garrett, 1972; Garrett and Munk, 1975), was systematically higher in 1/50° simulations, consistent with the idea that nonlinear interactions of internal gravity waves progressively fill out this spectral band (e.g., Olbers, 1976; McComas and Bretherton, 1977). This behavior reflects the ability of higher-resolution simulations to resolve the tidal peaks (Garrett and Munk, 1975) by resolving smaller-scale wave modes , which in turn increases the energy transferred

into the continuum (Müller et al., 2015). Nevertheless, even the higher-resolution simulations underestimate the continuum energy that feed the continuum through nonlinear wave–wave interactions (Müller et al., 2015). All simulations nevertheless underestimate this continuum relative to drifters. This mismatch , a mismatch that cannot be explained solely by the Eulerian–Lagrangian distinction , by the Eulerian-Lagrangian distinction and likely reflects both physical processes not fully represented in the models, such as parts of the incomplete wave–wave interaction cascade—and observational artifacts, because cascades in the models and a contribution of drifter positioning errors to the observed high-frequency variance in drifter records can be inflated by GPS/Argos positioning errors (Yu et al., 2019). In the open ocean, variance (Yu et al., 2019). Vertical resolution raises the total SHKE by +10% offshore and +13% on the shelf (Figure 11b), reflecting better-resolved horizontal flows via improved representation of their baroclinic structure (Stewart et al., 2017). This makes vertical resolution the parameter that generate the highest increase on the total shelf SHKE, ahead of horizontal resolution (+8%, Figure 11a). Higher-resolution bathymetry is the only parameter that reduces the total SHKE, and it does so on both subdomains (-7% offshore and -6% on the shelf, Figure 11e), because finer bathymetry both enhances lateral and bottom dissipation (Zhai et al., 2010; Ferrari and Wunsch, 2009) and reshapes the large-scale circulation through better-resolved bathymetric gradients (Chassignet and Xu, 2021; Chassignet et al., 2023).

Low frequencies (blue in Figure 11) dominate the offshore SHKE in both the simulations (83–93%of modeled KE lay at low frequencies versus) and the undrogued drifters (64–75% for undrogued drifters. There are not enough drifters to compare the observations to the models on the shelf78%), but there is astronger high frequency imprint in the models inshore than offshore, with the low-frequency KE accounting for only 45–50% inshore versus 83–93% offshore .

Second, we focused on the Lagrangian versus Eulerian perspective. Comparisons between numerical and undrogued drifters showed that numerical particles (OP) contain less total energy, but with a higher fraction of the total energy in consistent with large- and mesoscale motions carrying most of the semidiurnal band (from around 1.2%for undrogued surface drifters to 1.7% for OP) and in the near-inertial band (from around 5.8-5.9% for undrogued surface drifters to 7.6-8.1%for OP). Subsampling OP trajectories to match the drifter density slightly decreased the estimated KE–by just a few percent–indicating that, in the NEATL, sampling heterogeneity of surface buoys has a minor impact on the KE; this supports the use of surface drifters as a suitable reference dataset for model–data comparisons. Finally, OP–Eulerian comparisons confirmed that Lagrangian spectra are smoother, with attenuated oceanic kinetic energy (Wunsch and Stammer, 1995; Ferrari and Wunsch, 2009; Morrow and Le Traon, 2012). The smaller low-frequency fraction in the drifters reflects the richer high-frequency peaks and energy redistributed into surrounding frequencies, consistent with previous observational and modeling studies (e.g., ?Zhang et al., 2024). In our simulations, this smoothing led to around 50% less semidiurnal energy in Lagrangian than Eulerian estimates offshore.

Third, we conducted a pairwise sensitivity analysis to quantify the effect of specific model parameters on KE in both offshore (waters deeper than 500 m) and shelf (waters shallower than 500 m) regions. For the total KE, the dominant offshore factor was horizontal resolution: moving from 1/12° to 1/50° increased offshore KE by about one thirdcontent of their trajectories, at least partly attributable to measurement artifacts (Elipot et al., 2016; Yu et al., 2019; Arbic et al., 2022) and wind slippage (Niiler and Paduan, 1995; Arbic et al., 2022), rather than a deficit of absolute low-frequency energy. In absolute terms, NEATL50-T-HB-HF concentrates more low-frequency SHKE than the drifters in strong low-frequency motions, while the increase was less pronounced in the shelf region. By contrast, increasing vertical levels from drifters carry more low-frequency SHKE than the simulations in the weakly energetic basin interiors. We cannot explain these contrasts with our current model set-ups. Three parameters still carry a distinctive signature. Finer horizontal resolution strongly increases the low-frequency SHKE (+32to 96 raised the total KE in the shelf domain, but had a less pronounced impact in the offshore domain. Changes in

bathymetry resolution and wind forcing each have a slight impact on total energy, albeit in opposite directions: an increase in bathymetry resolution leads to a decrease in total energy, while an increase in wind forcing results in an energy increase.

Overall, the increase in total energy is evenly distributed between the % offshore and +17% on the shelf Figure 11a). Hourly wind forcing drops the offshore low-frequency reservoir and the remaining frequency domains. The only notable exception occurs when the wind forcing is increased from a 6-hour to a 1-hour interval. In this case, the percentage of total energy stored in low frequencies in the open ocean drops fraction from 91.4% to 86.7%, marking the only experiment where this percentage falls the only run below 90%. On the continental shelf, all the percentages consistently range between 45% and 50%. , through the same ratio effect as the drifter comparison, since the higher-frequency wind variability feeds the higher frequency continuum (Flexas et al., 2019) while leaving the absolute offshore low-frequency SHKE nearly unchanged ($<$1%, Figure 11f). Higher-resolution bathymetry reduces the low-frequency SHKE on both subdomains, more strongly on the shelf, likely reflecting the surface signature of an enhanced transfer of energy toward higher-frequency motions through flow–topography interactions and internal wave generation (e.g., Ferrari and Wunsch, 2009; Nikurashin and Ferrari, 2010; De Marez et al., 2020). Combined with the effect of finer bathymetry reduction of the total SHKE noted above, this suggests that at least part of the low-frequency energy removed from the surface is ultimately dissipated rather than transferred to higher frequencies.

For the diurnal frequency band, the most significant impact arises from the wind forcing. An increase in wind frequency doubles the fraction of total offshore energy contained in the diurnal band (from 1.1 to 2.4%) and, although less pronounced, also enhances it on the continental shelf(from 1.4 to 2.2%). This increase is expected near the diurnal NEATL50-T-HB-HF overestimates the observed drifter diurnal SHKE (green in Figure 11) equatorward of diurnal critical latitude (around i.e., 30°N) , where aliasing occurs between diurnal tides and near-inertial motions. However, the wind-frequency-induced enhancement of diurnal energy is not confined to the vicinity of the critical latitude but is observed across the entire NEATL domain. In contrast, considering only the and underestimates it poleward. Three parameters dominate this band in Figure 11. Hourly wind forcing more than doubles the offshore diurnal SHKE (+131%, Figure 11f) with a nearly uniform spatial pattern, consistent with the diurnal cycle of the wind (Dai and Deser, 1999; Savazzi et al., 2022; Dai, 2023). Expanding the tidal forcing from M_2 instead of eight largest tidal constituents (K_1, O_1, P_1, Q_1, monly to the eight largest constituents more than triples the diurnal SHKE on the shelf (+233%, Figure 11c), where the barotropic tidal currents are strongest (Pugh and Woodworth, 2014), while leaving the offshore signal poleward of 30°N nearly unchanged. Internal wave drag is absent following Xu et al. (2022), who adopted the Arbic et al. (2010) approach of tuning wave drag to fit observed tides and found that a zero drag scale minimizes the barotropic M_2 , S_2, N_2, and K_2) reduces this fraction on the continental shelf (from 1.5 to 0.5%) but not so much in the offshore region (from 1.3 to 1.1%).

For the semidiurnal frequency band, RMS error in NEATL tidal configuration. When reintroduced in NEATL50-T-WD, internal wave drag (Jayne and St. Laurent, 2001) acts on the diurnal band only equatorward of the most notable effect is the increase in the fraction of total energy stored in both the inshore (43.4 to 48.5%)and offshore (2 to 2.5%) domains when the bathymetry resolution is increaseddiurnal critical latitude (Figure 11d), consistent with its selective action on propagating internal tides. The poleward deficit in NEATL50-T-HB-HF diurnal SHKE is non-tidal, and among our tested parameters only increased wind forcing frequency acts on this signal. In contrast, and particularly in the offshore domain, the equatorward excess is of tidal origin, and the inclusion of a wave drag decreases the amount of energy stored (from 2% to 1.6%) in this band. Wave drag acts to reduce kinetic energy in all frequency bands equatorward of their respective critical latitudes and, because the semidiurnal critical latitude is located far poleward, this reduction is evident over nearly the entire domain. The decrease in semidiurnal energy associated with wave drag is consistent with weak

topographic wave drag as discussed in Xu et al. (2022) stands out as a concrete and testable path to bring the simulated diurnal SHKE closer to the drifter observations equatorward of 30°N.

In the semidiurnal band (orange in Figure 11), the distortion introduced by the Lagrangian sampling is the findings of Yu et al. (2019) and Arbic et al. (2022) who suggested that the absence of topographic internal wave drag can contribute to the overestimation of semidiurnal KE obtained with the MITgcm. largest (section 4) and prevents the use of the drifters as reference. Three parameters dominate this band in Figure 11. Higher-resolution bathymetry raises the semidiurnal SHKE on both subdomains despite reducing the total SHKE (Figure 11e), consistent with stronger barotropic-to-baroclinic conversion at a better-resolved shelf-break topography (Niwa and Hibiya, 2011; Buijsman et al., 2020; Xu et al., 2022), particularly clear for the well-known Amazon source of semidiurnal internal tides (Beardsley et al., 1995; Tchilibou et al., 2022). Finer horizontal resolution reduces the shelf semidiurnal fraction by -3% (Figure 11a), a change that seems small but is meaningful relative to the +8% shelf total increase, indicating enhanced shelf-break conversion that feeds internal tides radiating seaward, consistent with the predominantly barotropic nature of the shelf semidiurnal tide and with the dissipation of a large share of the global M_2 energy over continental shelves (Egbert and Ray, 2001). The corresponding +45% offshore increase is large in relative terms but represents only an absolute shift from 1.9% to 2.0% of the total SHKE. Yu et al. (2019) also suggested that insufficient horizontal resolution could enhance energy in the semidiurnal band by promoting the semidiurnal peak by inhibiting scattering into the wave continuum (Müller et al., 2015; Shriver et al., 2012). However, in our experiments, increasing resolution did not lead to a higher fraction of offshore total energy in the semidiurnal band, and in the shelf domain; it actually resulted in a reduction in the fraction of total energy stored in this band. (Müller et al., 2015; Shriver et al., 2012). This mechanism could additionally contribute to the shelf semidiurnal reduction, but raises the question of why a comparable reduction is not apparent in the deep ocean. Internal wave drag cuts the offshore semidiurnal SHKE by about one quarter (-27%) while barely affecting the total (Figure 11d), in line with the interpretation of Yu et al. (2019) and Arbic et al. (2022) that the semidiurnal excess in tide-forced models reflects in part the absence of such a drag. This reduction is spatially concentrated away from the Gulf of Mexico-Gulf Stream pathway, suggesting a weaker imprint of wave drag in regions of strong western boundary currents. The excess in semidiurnal SHKE in OP Seed drifters when compared to measurements is predominantly in the deep ocean, exactly where wave drag preferentially acts. As for the diurnal band, adding a weak topographic wave drag may bring the simulated semidiurnal SHKE closer to the drifter observations, damping the model excess in the deep ocean without altering the western boundary current signal.

Finally, for Finally, in the near-inertial frequency band, primarily associated with anticyclonic motion, band (red in Figure 11) , the most significant factor is the increase in wind forcing frequency, which nearly doubles the fraction of energy stored in drifters carry more SHKE than NEATL50-T-HB-HF over the same regions of strong low-frequency motions as in the semidiurnal band as well as near the low-latitude equatorial edge of the band. Two parameters dominate this band in the open ocean Figure 11. Hourly wind forcing nearly doubles the offshore near-inertial fraction (from 4.5% to 7.6%) and only slightly inshore (from 18.5 to 19.3%), , corresponding to a +80% absolute increase, Figure 11f), and produces a more modest rise on the shelf, consistent with winds being a major source of near-inertial motions (Klein et al., 2004; Rimac et al., 2013)(Klein et al., 2004; Rimac et al., 2013). As noted by Rimac et al. (2013) and Yu et al. (2019), this increase is less pronounced in tropical and subtropical regions than at mid-latitudes. In contrast, an increase in horizontal resolution , although associated with a higher absolute energy in this band due to the overall rise in total energy, reduces Finer horizontal resolution

acts in the opposite direction. Although the absolute near-inertial SHKE rises along with the overall SHKE increase, the fraction of total energy stored in the near-inertial band in the offshore region SHKE stored in this band drops (Figure 11a) both offshore (from 6.1% of total SHKE to 4.2%) and in the shelf domain (on the shelf (from 20.3% of total SHKE to 18%). A natural interpretation would invoke a more efficient vertical transport of near-inertial kinetic energy into the ocean interior through the better-resolved mesoscale and submesoscale fields (e.g., Kunze, 1985; Thomas et al., 2020; Lu et al., 2023). However, the spatial pattern does not straightforwardly support this view, since the reduction is not systematically concentrated in the most energetic regions of the domain but rather appears in the basin interior, leaving the origin of this near-inertial deficit at higher resolution as an open question.

In conclusion, this study used six pairwise twin experiments, each isolating a single numerical choice, to quantify how individual model parameters shape the surface horizontal kinetic energy (SHKE) distribution in the North and Equatorial Atlantic. Earlier comparisons of SHKE in tide-resolving models to drifter observations (Yu et al., 2019; Arbic et al., 2022) have raised a number of hypotheses on the role of individual parameters in shaping the SHKE distribution, but these hypotheses could not be directly tested because the model pairs they compared differed in several parameters simultaneously. Our twin-experiment design addresses this limitation by changing only one parameter at a time across a dedicated suite of tide-resolving, eddy-resolving to submesoscale-permitting simulations. Although several questions remain open, the design has made it possible to carry out a parameter-by-parameter assessment of the SHKE distribution within a unified diagnostic framework and frequency decomposition, providing a by-band, by-subdomain view of the individual effects of each parameter on the SHKE. This sensitivity picture should be of practical use to anyone designing a future tide-resolving numerical simulation. For the HYCOM NEATL configuration, the natural next step would be to test the inclusion of a topographic internal wave drag in NEATL50-T-HB-HF, which should reduce the tidal-band SHKE excess relative to the drifters equatorward of the respective critical latitudes. The twin-experiment framework could also be extended toward parameters still left untested here, with a particular focus on the mechanisms able to amplify the non-tidal variability away from the low-frequency motions. Two natural candidates are the lateral viscosity and the wind stress formulation, both recently shown to substantially modulate the Gulf Stream pathway and variability in a non-tidal NEATL50 simulation by Chassignet and Xu (2025).

Code and data availability. The HYCOM 2.3.01 source code is available at https://github.com/HYCOM/HYCOM-src/tree/2.3.01 and is archived at SEANOE (doi:10.17882/111296; Laxenaire et al., 2026). The full-resolution HYCOM model outputs are stored in the U.S. Army Engineer Research and Development Center (ERDC) and U.S. Navy DoD Supercomputing Resource Center (DSRC) archive servers and are available on request. The Parcels Python package used in this study (v2.3.2) is archived on Zenodo (doi:10.5281/zenodo.7035503; Van Sebille et al., 2021). Version 2.01 of the hourly Global Drifter Program dataset (Elipot et al., 2016, 2022) was downloaded on 30 April 2025, and an archived copy of the subset used in this study is available at SEANOE (doi:10.17882/111296; Laxenaire et al., 2026). The gridded $1^\circ \times 1^\circ$ rotary surface velocity spectra and derived kinetic energy diagnostics (total, low-frequency, diurnal, semidiurnal, and near-inertial) for the seven HYCOM NEATL simulations, the OceanParcels experiments, and the four drifter datasets (drogued or undrogued; all positions or GPS only), together with an M-language script to reproduce the figures of this paper (compatible with both MATLAB and GNU

Octave), are archived at SEANOE (doi:10.17882/111296; Laxenaire et al., 2026). Beyond reproducing the figures, the interested reader can zoom into specific regions or frequency bands of the sensitivity results, and can also step outside the strict single-parameter design adopted here by combining pairs of experiments to probe the joint effect of two parameters at once.

Author contributions. RL, EC, MB, and BA conceived and proposed the idea for this study. XX ran the numerical simulations and the OceanParcels Experiments. RL did the analysis. RL and EC wrote the first draft of the manuscripts. All authors contributed to the writing and editing of the manuscript.

Competing interests. The authors declare that they have no conflict of interest.

Acknowledgements. Shane Elipot was supported by US National Science Foundation (NSF) Grants OCE-2242111 and OCE-1851166, Brian Arbic by the Office of Naval Research (ONR) Grant N00014-19-1-2712, Maarten Buijsman and Miguel Solano by the ONR Grant N00014-19-1-2704, and Eric Chassignet, Xiaobiao Xu, Alan Wallcraft, Luna Hiron, and Rémi Laxenaire by the ONR Grant N00014-19-1-2717. The seven HYCOM simulations were performed on supercomputers at the U.S. Army Engineer Research and Development Center (ERDC) in Vicksburg, Mississippi, and the US Navy DoD Super-computing Resource Center (DSRC) in Stennis Space Center, Mississippi, using computer time provided by the US DoD High Performance Computing Modernization Program.

References

Abdalla, S., Kolahchi, A. A., Ablain, M., Adusumilli, S., Bhowmick, S. A., Alou-Font, E., Amarouche, L., Andersen, O. B., Antich, H., Aouf, L., et al.: Altimetry for the future: Building on 25 years of progress, Advances in Space Research, 68, 319–363, https://doi.org/10.1016/j.asr.2021.01.022, 2021.

Ajayi, A., Le Sommer, J., Chassignet, E., Molines, J.-M., Xu, X., Albert, A., and Cosme, E.: Spatial and Temporal Variability of the North Atlantic Eddy Field From Two Kilometric-Resolution Ocean Models, Journal of Geophysical Research: Oceans, 125, e2019JC015 827, https://doi.org/10.1029/2019JC015827, 2020.

Ajayi, A., Le Sommer, J., Chassignet, E. P., Molines, J.-M., Xu, X., Albert, A., and Dewar, W.: Diagnosing Cross-Scale Kinetic Energy Exchanges From Two Submesoscale Permitting Ocean Models, Journal of Advances in Modeling Earth Systems, 13, e2019MS001 923, https://doi.org/10.1029/2019MS001923, 2021.

Amante, C. and Eakins, B.: ETOPO1 1 Arc-Minute Global Relief Model: procedures, data sources and analysis, NOAA Technical Memorandum NESDIS NGDC-24. National Geophysical Data Center, NOAA., https://doi.org/10.7289/V5C8276M, 2009.

Ansong, J. K., Arbic, B. K., Buijsman, M. C., Richman, J. G., Shriver, J. F., and Wallcraft, A. J.: Indirect evidence for substantial damping of low-mode internal tides in the open ocean, Journal of Geophysical Research: Oceans, 120, 6057–6071, https://doi.org/10.1002/2015JC010998, 2015.

Arbic, B. K.: Incorporating tides and internal gravity waves within global ocean general circulation models: A review, Progress in Oceanography, 206, 102 824, https://doi.org/10.1016/j.pocean.2022.102824, 2022.

Arbic, B. K., Wallcraft, A. J., and Metzger, E. J.: Concurrent simulation of the eddying general circulation and tides in a global ocean model, Ocean Modelling, 32, 175–187, https://doi.org/10.1016/j.ocemod.2010.01.007, 2010.

Arbic, B. K., Richman, J. G., Shriver, J. F., Timko, P. G., Metzger, E. J., and Wallcraft, A. J.: Global modeling of internal tides: Within an eddying ocean general circulation model, Oceanography, 25, 20–29, https://doi.org/0.5670/oceanog.2012.38, 2012.

Arbic, B. K., Alford, M. H., Ansong, J. K., Buijsman, M. C., Ciotti, R. B., Farrar, J. T., Hallberg, R. W., Henze, C. E., Hill, C. N., Luecke, C. A., et al.: A primer on global internal tide and internal gravity wave continuum modeling in HYCOM and MITgcm, New frontiers in operational oceanography, https://doi.org/10.17125/gov2018.ch13, 2018.

Arbic, B. K., Elipot, S., Brasch, J. M., Menemenlis, D., Ponte, A. L., Shriver, J. F., Yu, X., Zaron, E. D., Alford, M. H., Buijsman, M. C., et al.: Near-surface oceanic kinetic energy distributions from drifter observations and numerical models, Journal of Geophysical Research: Oceans, 127, e2022JC018 551, https://doi.org/10.1029/2022JC018551, 2022.

Archer, M., Wang, J., Klein, P., Dibarboure, G., and Fu, L.-L.: Wide-swath satellite altimetry unveils global submesoscale ocean dynamics, Nature, 640, 691–696, https://doi.org/10.1038/s41586-025-08722-8, 2025.

Baumann, T. M., Polyakov, I. V., Padman, L., Danielson, S., Fer, I., Janout, M., Williams, W., and Pnyushkov, A. V.: Arctic tidal current atlas, Scientific Data, 7, 275, https://doi.org/10.1038/s41597-020-00578-z, 2020.

Beardsley, R. C., Candela, J., Limeburner, R., Geyer, W. R., Lentz, S. J., Castro, B. M., Cacchione, D., and Carneiro, N.: The M2 tide on the Amazon Shelf, Journal of Geophysical Research: Oceans, 100, 2283–2319, https://doi.org/10.1029/94JC01688, 1995.

Bleck, R.: An oceanic general circulation model framed in hybrid isopycnic-Cartesian coordinates, Ocean Modelling, 4, 55 – 88, https://doi.org/10.1016/S1463-5003(01)00012-9, 2002.

Buijsman, M. C., Arbic, B. K., Green, J., Helber, R. W., Richman, J. G., Shriver, J. F., Timko, P., and Wallcraft, A.: Optimizing internal wave drag in a forward barotropic model with semidiurnal tides, Ocean Modelling, 85, 42–55, https://doi.org/10.1016/j.ocemod.2014.11.003, 2015.

Buijsman, M. C., Stephenson, G. R., Ansong, J. K., Arbic, B. K., Green, J. M., Richman, J. G., Shriver, J. F., Vic, C., Wallcraft, A. J., and Zhao, Z.: On the interplay between horizontal resolution and wave drag and their effect on tidal baroclinic mode waves in realistic global ocean simulations, Ocean Modelling, 152, 101 656, https://doi.org/10.1016/j.ocemod.2020.101656, 2020.

Buijsman, M. C., Abdulfatai, M., Arbic, B. K., Chassignet, E. P., Hiron, L., Shriver, J. F., Solano, M., Varma, D., and Xu, X.: Energetics of (Super)Tidal Baroclinic Modes in a Realistically Forced Global Ocean Simulation, Journal of Geophysical Research: Oceans, 130, e2025JC022 460, https://doi.org/10.1029/2025JC022460, 2025.

Carnes, M. R.: Description and evaluation of GDEMV 3.0. Naval Rearch Laboratory Memo, Tech. rep., NRL/MR/7330-09-9165, 2009.

Caspar-Cohen, Z., Ponte, A., Lahaye, N., Carton, X., Yu, X., and Legentil, S.: Characterization of Internal Tide Incoherence: Eulerian versus Lagrangian Perspectives, Journal of Physical Oceanography, 52, 1245 – 1259, https://doi.org/10.1175/JPO-D-21-0088.1, 2022.

Caspar-Cohen, Z., Ponte, A., Lahaye, N., Zaron, E. D., Arbic, B. K., Yu, X., LeGentil, S., and Menemenlis, D.: Combining surface drifters and high resolution global simulations enables the mapping of internal tide surface energy, Scientific Reports, 15, 10 672, https://doi.org/10.1038/s41598-025-92662-w, 2025.

Chassignet, E. P. and Xu, X.: Impact of horizontal resolution (1/12 to 1/50) on Gulf Stream separation, penetration, and variability, Journal of Physical Oceanography, 47, 1999–2021, https://doi.org/10.1175/JPO-D-17-0031.1, 2017.

Chassignet, E. P. and Xu, X.: On the importance of high-resolution in large-scale ocean models, Advances in Atmospheric Sciences, 38, 1621–1634, https://doi.org/10.1007/s00376-021-0385-7, 2021.

Chassignet, E. P. and Xu, X.: Impact of wind stress formulation on Gulf Stream pathway and variability, Frontiers in Marine Science, 12, 1739 630, https://doi.org/10.3389/fmars.2025.1739630, 2025.

Chassignet, E. P., Smith, L. T., Halliwell, G. R., and Bleck, R.: North Atlantic Simulations with the Hybrid Coordinate Ocean Model (HYCOM): Impact of the Vertical Coordinate Choice, Reference Pressure, and Thermobaricity, Journal of Physical Oceanography, 33, 2504–2526, https://doi.org/10.1175/1520-0485(2003)033<2504:naswth>2.0.co;2, 2003.

Chassignet, E. P., Hurlburt, H. E., Smedstad, O. M., Halliwell, G. R., Wallcraft, A. J., Metzger, E. J., Blanton, B. O., Lozano, C., Rao, D. B., Hogan, P. J., et al.: Generalized vertical coordinates for eddy-resolving global and coastal ocean forecasts, OCEANOGRAPHY-WASHINGTON DC-OCEANOGRAPHY SOCIETY-, 19, 118, https://doi.org/10.5670/oceanog.2006.95, 2006.

Chassignet, E. P., Hurlburt, H. E., Metzger, E. J., Smedstad, O. M., Cummings, J. A., Halliwell, G. R., Bleck, R., Baraille, R., Wallcraft, A. J., Lozano, C., Tolman, H. L., Srinivasan, A., Hankin, S., Cornillon, P., Weisberg, R., Barth, A., He, R., Werner, F., and Wilkin, J.: US GODAE: Global Ocean Prediction with the HYbrid Coordinate Ocean Model (HYCOM), Oceanography, 22, 64–75, https://doi.org/10.5670/oceanog.2009.39, 2009.

Chassignet, E. P., Yeager, S. G., Fox-Kemper, B., Bozec, A., Castruccio, F., Danabasoglu, G., Kim, W. M., Koldunov, N., Li, Y., and Lin, P.: Impact of horizontal resolution on global ocean-sea-ice model simulations based on the experimental protocols of the Ocean Model Intercomparison Project phase 2 (OMIP-2), Geoscientific Model Development Discussions, 2020, 1–58, https://doi.org/10.5194/gmd-13-4595-2020, 2020.

Chassignet, E. P., Xu, X., Bozec, A., and Uchida, T.: Impact of the New England seamount chain on Gulf Stream pathway and variability, Journal of Physical Oceanography, 53, 1871–1886, https://doi.org/10.1175/JPO-D-23-0008.1, 2023.

Chelton, D. B., Schlax, M. G., and Samelson, R. M.: Global observations of nonlinear mesoscale eddies, Progress in Oceanography, 91, 167–216, https://doi.org/10.1016/j.pocean.2011.01.002, 2011.

Cummins, P. F., Karsten, R. H., and Arbic, B. K.: The semi-diurnal tide in Hudson strait as a resonant channel oscillation, Atmosphere-ocean, 48, 163–176, https://doi.org/10.3137/OC307.2010, 2010.

Dai, A.: The diurnal cycle from observations and ERA5 in surface pressure, temperature, humidity, and winds, Climate Dynamics, 61, 2965–2990, https://doi.org/s00382-023-06721-x, 2023.

Dai, A. and Deser, C.: Diurnal and semidiurnal variations in global surface wind and divergence fields, Journal of Geophysical Research: Atmospheres, 104, 31 109–31 125, https://doi.org/10.1029/1999JD900927, 1999.

Davis, R.: Oceanic property transport, Lagrangian particle statistics, and their prediction, Journal of Marine Research, 41, 163–194, 1983.

De Marez, C., Lahaye, N. J., and Gula, J.: Interaction of the Gulf Stream with small scale topography: A focus on lee waves, Scientific Reports, 10, 2332, https://doi.org/10.1038/s41598-020-59297-5, 2020.

Delandmeter, P. and Van Sebille, E.: The Parcels v2. 0 Lagrangian framework: new field interpolation schemes, Geoscientific Model Development, 12, 3571–3584, https://doi.org/10.5194/gmd-12-3571-2019, 2019.

Egbert, G. D. and Ray, R. D.: Estimates of M2 tidal energy dissipation from TOPEX/Poseidon altimeter data, Journal of Geophysical Research: Oceans, 106, 22 475–22 502, https://doi.org/10.1029/2000JC000699, 2001.

Elipot, S. and Lumpkin, R.: Spectral description of oceanic near-surface variability, Geophysical Research Letters, 35, https://doi.org/10.1029/2007GL032874, 2008.

Elipot, S., Lumpkin, R., Perez, R. C., Lilly, J. M., Early, J. J., and Sykulski, A. M.: A global surface drifter data set at hourly resolution, Journal of Geophysical Research: Oceans, 121, 2937–2966, https://doi.org/10.1002/2016JC011716, 2016.

Elipot, S., Sykulski, A., Lumpkin, R., Centurioni, L., and Pazos, M.: Hourly location, current velocity, and temperature collected from Global Drifter Program drifters world-wide, Accession, 248584, v1, https://doi.org/10.25921/x46c-3620, 2022.

Emery, W. J. and Thomson, R. E.: Data Analysis Methods in Physical Oceanography (Second and Revised ed.), Elsevier, 2001.

Ferrari, R. and Wunsch, C.: Ocean circulation kinetic energy: Reservoirs, sources, and sinks, Annual Review of Fluid Mechanics, 41, https://doi.org/10.1146/annurev.fluid.40.111406.102139, 2009.

Flexas, M. M., Thompson, A. F., Torres, H. S., Klein, P., Farrar, J. T., Zhang, H., and Menemenlis, D.: Global estimates of the energy transfer from the wind to the ocean, with emphasis on near-inertial oscillations, Journal of Geophysical Research: Oceans, 124, 5723–5746, https://doi.org/10.1029/2018JC014453, 2019.

Fratantoni, D. M. and Glickson, D. A.: North Brazil Current ring generation and evolution observed with SeaWiFS, Journal of Physical Oceanography, 32, 1058–1074, https://doi.org/10.1175/1520-0485(2002)032<1058:NBCRGA>2.0.CO;2, 2002.

Fu, L.-L., Pavelsky, T., Cretaux, J.-F., Morrow, R., Farrar, J. T., Vaze, P., Sengenes, P., Vinogradova-Shiffer, N., Sylvestre-Baron, A., Picot, N., and Dibarboure, G.: The Surface Water and Ocean Topography Mission: A Breakthrough in Radar Remote Sensing of the Ocean and Land Surface Water, Geophysical Research Letters, 51, e2023GL107 652, https://doi.org/10.1029/2023GL107652, 2024.

Furevik, T. and Foldvik, A.: Stability at M2 critical latitude in the Barents Sea, Journal of Geophysical Research: Oceans, 101, 8823–8837, https://doi.org/10.1029/96JC00081, 1996.

Gabioux, M., Vinzon, S. B., and Paiva, A. M.: Tidal propagation over fluid mud layers on the Amazon shelf, Continental Shelf Research, 25, 113–125, https://doi.org/10.1016/j.csr.2004.09.001, 2005.

Garrett, C.: Tidal resonance in the Bay of Fundy and Gulf of Maine, Nature, 238, 441–443, https://doi.org/10.1038/238441a0, 1972.

Garrett, C. and Munk, W.: Space-time scales of internal waves: A progress report, Journal of Geophysical Research, 80, 291–297, https://doi.org/10.1029/JC080i003p00291, 1975.

GEBCO Bathymetric Compilation Group 2019: The GEBCO_2019 Grid - a continuous terrain model of the global oceans and land. British Oceanographic Data Centre, National Oceanography Centre, NERC, UK, https://doi.org/10.5285/836f016a-33be-6ddc-e053-6c86abc0788e, 2019.

Goerss, J. S. and Jeffries, R. A.: Assimilation of synthetic tropical cyclone observations into the Navy Operational Global Atmospheric Prediction System, Weather and forecasting, 9, 557–576, https://doi.org/10.1175/1520-0434(1994)009<0557:AOSTCO>2.0.CO;2, 1994.

Gonella, J.: A rotary-component method for analysing meteorological and oceanographic vector time series, Deep Sea Research and Oceanographic Abstracts, 19, 833–846, https://doi.org/10.1016/0011-7471(72)90002-2, 1972.

Gouillon, F., Morey, S. L., Dukhovskoy, D. S., and O'Brien, J. J.: Forced tidal response in the Gulf of Mexico, Journal of Geophysical Research: Oceans, 115, https://doi.org/10.1029/2010JC006122, 2010.

Grace, S. F.: The Principal Diurnal Constituent of Tidal Motion in the Gulf of Mexico., Geophysical Journal International, 3, 70–83, https://doi.org/10.1111/j.1365-246X.1932.tb00401.x, 1932.

Hiron, L., Schönau, M. C., Raja, K. J., Chassignet, E. P., Buijsman, M. C., Arbic, B. K., Bozec, A., Coelho, E. F., and Solano, M. S.: The Influence of Vertical Resolution on Internal Tide Energetics and Subsequent Effects on Underwater Acoustic Propagation, Journal of Advances in Modeling Earth Systems, 17, e2024MS004 389, https://doi.org/10.1029/2024MS004389, e2024MS004389 2024MS004389, 2025.

Hogan, T. F. and Rosmond, T. E.: The description of the Navy Operational Global Atmospheric Prediction System's spectral forecast model, Monthly Weather Review, 119, 1786–1815, https://doi.org/10.1175/1520-0493(1991)119<1786:TDOTNO>2.0.CO;2, 1991.

Jayne, S. R. and St. Laurent, L. C.: Parameterizing tidal dissipation over rough topography, Geophysical Research Letters, 28, 811–814, https://doi.org/10.1029/2000GL012044, 2001.

Jänicke, L., Ebener, A., Dangendorf, S., Arns, A., Schindelegger, M., Niehüser, S., Haigh, I. D., Woodworth, P., and Jensen, J.: Assessment of Tidal Range Changes in the North Sea From 1958 to 2014, Journal of Geophysical Research: Oceans, 126, e2020JC016 456, https://doi.org/10.1029/2020JC016456, 2021.

Klein, P., Lapeyre, G., and Large, W. G.: Wind ringing of the ocean in presence of mesoscale eddies, Geophysical Research Letters, 31, https://doi.org/10.1029/2004GL020274, 2004.

Kunze, E.: Near-Inertial Wave Propagation In Geostrophic Shear, Journal of Physical Oceanography, 15, 544 – 565, https://doi.org/10.1175/1520-0485(1985)015<0544:NIWPIG>2.0.CO;2, 1985.

Lange, M. and Van Sebille, E.: Parcels v0. 9: prototyping a Lagrangian ocean analysis framework for the petascale age, Geoscientific Model Development, 10, 4175–4186, https://doi.org/10.5194/gmd-10-4175-2017, 2017.

Laxenaire, R., Chassignet, E. P., and Xu, X.: Gridded rotary velocity spectra and surface kinetic energy in the North and Equatorial Atlantic from HYCOM NEATL simulations, OceanParcels trajectories, and GDP drifter observations. SEANOE, https://doi.org/10.17882/111296, 2026.

Le Traon, P.-Y.: From satellite altimetry to Argo and operational oceanography: three revolutions in oceanography, Ocean Science, 9, 901–915, https://doi.org/10.5194/os-9-901-2013, 2013.

Leben, R. R.: Altimeter-Derived Loop Current Metrics, pp. 181–201, American Geophysical Union (AGU), ISBN 9781118666166, https://doi.org/10.1029/161GM15, 2005.

Lu, X., Dong, C., Xu, Z., Yang, J., Zhang, H., Wang, D., and Chen, D.: Effects of Numerical Model's Horizontal Resolution on the Vertical Transport of Near-Inertial Energy, Deep Sea Research Part II: Topical Studies in Oceanography, 207, 105 223, https://doi.org/10.1016/j.dsr2.2022.105223, 2023.

Lumpkin, R. and Pazos, M.: Measuring surface currents with Surface Velocity Program drifters: the instrument, its data, and some recent results, in: Lagrangian Analysis and Prediction of Coastal and Ocean Dynamics, edited by Griffa, A., Kirwan, A. D., J., Mariano, A. J., Özgökmen, T., and Rossby, H. T., pp. 39–67, Cambridge University Press, Cambridge, https://doi.org/10.1017/CBO9780511535901.003, 2007.

McComas, C. H. and Bretherton, F. P.: Resonant interaction of oceanic internal waves, Journal of Geophysical Research, 82, 1397–1412, https://doi.org/10.1029/JC082i009p01397, 1977.

Middleton, J. F.: Drifter spectra and diffusivities, Journal of marine research, 43, 37–55, 1985.

Middleton, J. H. and Denniss, T.: The propagation of tides near the critical latitude, Geophysical & Astrophysical Fluid Dynamics, 68, 1–13, https://doi.org/10.1080/03091929308203559, 1993.

Mooers, C. N.: A technique for the cross spectrum analysis of pairs of complex-valued time series, with emphasis on properties of polarized components and rotational invariants, Deep Sea Research and Oceanographic Abstracts, 20, 1129–1141, https://doi.org/10.1016/0011-7471(73)90027-2, 1973.

Morrow, R. and Le Traon, P.-Y.: Recent advances in observing mesoscale ocean dynamics with satellite altimetry, Advances in Space Research, 50, 1062–1076, https://doi.org/10.1016/j.asr.2011.09.033, 2012.

Morrow, R., Fu, L.-L., Ardhuin, F., Benkiran, M., Chapron, B., Cosme, E., d'Ovidio, F., Farrar, J. T., Gille, S. T., Lapeyre, G., et al.: Global observations of fine-scale ocean surface topography with the Surface Water and Ocean Topography (SWOT) mission, Frontiers in Marine Science, 6, 232, https://doi.org/10.3389/fmars.2019.00232, 2019.

Müller, P., McWilliams, J., and Molemaker, M.: Routes to dissipation in the ocean: The 2D/3D turbulence conundrum, Marine turbulence: theories, observations and models, 397, 405, 2005.

Müller, M., Arbic, B. K., Richman, J. G., Shriver, J. F., Kunze, E. L., Scott, R. B., Wallcraft, A. J., and Zamudio, L.: Toward an internal gravity wave spectrum in global ocean models, Geophysical Research Letters, 42, 3474–3481, https://doi.org/10.1002/2015GL063365, 2015.

Nelson, A., Arbic, B., Menemenlis, D., Peltier, W., Alford, M., Grisouard, N., and Klymak, J.: Improved internal wave spectral continuum in a regional ocean model, Journal of Geophysical Research: Oceans, 125, e2019JC015 974, https://doi.org/10.1029/2019JC015974, 2020.

Niiler, P. P. and Paduan, J. D.: Wind-Driven Motions in the Northeast Pacific as Measured by Lagrangian Drifters, Journal of Physical Oceanography, 25, 2819 – 2830, https://doi.org/10.1175/1520-0485(1995)025<2819:WDMITN>2.0.CO;2, 1995.

Nikurashin, M. and Ferrari, R.: Radiation and dissipation of internal waves generated by geostrophic motions impinging on small-scale topography: Theory, Journal of Physical Oceanography, 40, 1055–1074, https://doi.org/10.1175/2009JPO4199.1, 2010.

Niwa, Y. and Hibiya, T.: Estimation of Baroclinic Tide Energy Available for Deep Ocean Mixing Based on Three-Dimensional Global Numerical Simulations, Journal of Oceanography, 67, 493–502, https://doi.org/10.1007/s10872-011-0052-1, 2011.

Olbers, D. J.: Nonlinear energy transfer and the energy balance of the internal wave field in the deep ocean, Journal of Fluid mechanics, 74, 375–399, https://doi.org/10.1017/S0022112076001857, 1976.

Pugh, D. and Woodworth, P.: Tidal dynamics, p. 97–132, Cambridge University Press, 2014.

Raja, K. J., Buijsman, M. C., Shriver, J. F., Arbic, B. K., and Siyanbola, O.: Near-inertial wave energetics modulated by background flows in a global model simulation, Journal of Physical Oceanography, 52, 823–840, https://doi.org/10.1175/JPO-D-21-0130.1, 2022.

Ray, R. D.: Propagation of the overtide M4 through the deep Atlantic Ocean, Geophysical Research Letters, 34, https://doi.org/10.1029/2007GL031618, 2007.

Rimac, A., von Storch, J.-S., Eden, C., and Haak, H.: The influence of high-resolution wind stress field on the power input to near-inertial motions in the ocean, Geophysical Research Letters, 40, 4882–4886, https://doi.org/10.1002/grl.50929, 2013.

Robertson, R.: Internal tides and baroclinicity in the Southern Weddell Sea: 2. Effects of the critical latitude and stratification, Journal of Geophysical Research: Oceans, 106, 27 017–27 034, https://doi.org/10.1029/2000JC000476, 2001.

Saha, S., Moorthi, S., Pan, H.-L., Wu, X., Wang, J., Nadiga, S., Tripp, P., Kistler, R., Woollen, J., Behringer, D., and et al.: The NCEP Climate Forecast System Reanalysis, Bulletin of the American Meteorological Society, 91, 1015–1058, https://doi.org/10.1175/2010bams3001.1, 2010.

Savazzi, A. C. M., Nuijens, L., Sandu, I., George, G., and Bechtold, P.: The representation of the trade winds in ECMWF forecasts and reanalyses during EUREC4A, Atmospheric Chemistry and Physics, 22, 13 049–13 066, https://doi.org/10.5194/acp-22-13049-2022, 2022.

Shriver, J. F., Arbic, B. K., Richman, J. G., Ray, R. D., Metzger, E. J., Wallcraft, A. J., and Timko, P. G.: An evaluation of the barotropic and internal tides in a high-resolution global ocean circulation model, Journal of Geophysical Research: Oceans, 117, https://doi.org/10.1029/2012JC008170, 2012.

Smith, W. and Sandwell, D.: Global Sea Floor Topography from Satellite Altimetry and Ship Depth Soundings, Science, 277, 1956–1962, https://doi.org/10.1126/science.277.5334.1956, 1997.

Stewart, K., Hogg, A. M., Griffies, S., Heerdegen, A., Ward, M., Spence, P., and England, M. H.: Vertical resolution of baroclinic modes in global ocean models, Ocean Modelling, 113, 50–65, https://doi.org/10.1016/j.ocemod.2017.03.012, 2017.

Tchilibou, M., Koch-Larrouy, A., Barbot, S., Lyard, F., Morel, Y., Jouanno, J., and Morrow, R.: Internal tides off the Amazon shelf during two contrasted seasons: interactions with background circulation and SSH imprints, Ocean Science, 18, 1591–1618, https://doi.org/10.5194/os-18-1591-2022, 2022.

Teague, W. J., Carron, M. J., and Hogan, P. J.: A comparison between the Generalized Digital Environmental Model and Levitus climatologies, Journal of Geophysical Research: Oceans, 95, 7167–7183, https://doi.org/10.1029/JC095iC05p07167, 1990.

Thomas, L. N., Rainville, L., Asselin, O., Young, W. R., Girton, J., Whalen, C. B., Centurioni, L., and Hormann, V.: Direct Observations of Near-Inertial Wave ζ-Refraction in a Dipole Vortex, Geophysical Research Letters, 47, e2020GL090 375, https://doi.org/10.1029/2020GL090375, 2020.

Uppala, S. M., Kållberg, P., Simmons, A. J., Andrae, U., Bechtold, V. D. C., Fiorino, M., Gibson, J., Haseler, J., Hernandez, A., Kelly, G., et al.: The ERA-40 re-analysis, Quarterly Journal of the Royal Meteorological Society: A journal of the atmospheric sciences, applied meteorology and physical oceanography, 131, 2961–3012, https://doi.org/10.1256/qj.04.176, 2005.

Van Sebille, E., Kehl, C., Lange, M., Delandmeter, P., and contributors, T. P.: Parcels, https://doi.org/10.5281/zenodo.7035503, 2021.

Villas Bôas, A. B., Marechal, G., and Bohé, A.: Observing Interactions Between Waves, Winds, and Currents From SWOT, Geophysical Research Letters, 52, e2024GL114 331, https://doi.org/10.1029/2024GL114331, 2025.

Webb, D. J.: On the shelf resonances of the English Channel and Irish Sea, Ocean Science, 9, 731–744, https://doi.org/10.5194/os-9-731-2013, 2013.

Wunsch, C. and Ferrari, R.: Vertical mixing, energy, and the general circulation of the oceans, Annu. Rev. Fluid Mech., 36, 281–314, https://doi.org/10.1146/annurev.fluid.36.050802.122121, 2004.

Wunsch, C. and Stammer, D.: The global frequency-wavenumber spectrum of oceanic variability estimated from TOPEX/POSEIDON altimetric measurements, Journal of Geophysical Research: Oceans, 100, 24 895–24 910, https://doi.org/10.1029/95JC017830, 1995.

Xu, X., Chassignet, E. P., Wallcraft, A. J., Arbic, B. K., Buijsman, M. C., and Solano, M.: On the spatial variability of the mesoscale sea surface height wavenumber spectra in the Atlantic Ocean, Journal of Geophysical Research: Oceans, 127, e2022JC018 769, https://doi.org/10.1029/2022JC018769, 2022.

Xu, X., Chassignet, E. P., and Wallcraft, A. J.: Impact of vertical resolution on representing baroclinic modes and water mass distribution in the North Atlantic, Ocean Modelling, 186, 102 261, https://doi.org/10.1016/j.ocemod.2023.102261, 2023.

Yu, X., Ponte, A. L., Elipot, S., Menemenlis, D., Zaron, E. D., and Abernathey, R.: Surface kinetic energy distributions in the global oceans from a high-resolution numerical model and surface drifter observations, Geophysical Research Letters, 46, 9757–9766, https://doi.org/10.1029/2019GL083074, 2019.

Zaron, E. D. and Elipot, S.: An assessment of global ocean barotropic tide models using geodetic mission altimetry and surface drifters, Journal of Physical Oceanography, 51, 63–82, https://doi.org/10.1175/JPO-D-20-0089.1, 2021.

Zhai, X., Johnson, H. L., and Marshall, D. P.: Significant sink of ocean-eddy energy near western boundaries, Nature Geoscience, 3, 608–612, https://doi.org/10.1038/ngeo943, 2010.

Zhang, X., Yu, X., Ponte, A. L., Caspar-Cohen, Z., Le Gentil, S., Wang, L., and Gong, W.: Lagrangian Versus Eulerian Spectral Estimates of Surface Kinetic Energy Over the Global Ocean, Journal of Geophysical Research: Oceans, 129, e2024JC021 057, https://doi.org/doi.org/10.1029/2024JC021057, e2024JC021057 2024JC021057, 2024.